PASCAL

# D13
# Sloshing CFD modeling and validation with SHAKESPEARE first experimental campaign

V. Moreau & M. Profir (CRS4)

Version 1 - 12/07/2023

The PASCAL project has received funding from the EURATOM research and training programme 2014-2020 under Grant Agreement No 945341.

# Document properties

| | |
|---|---|
| Title: | Sloshing CFD modeling and validation with SHAKESPEARE first experimental campaign |
| Type: | R (Deliverable) |
| Number: | D13 |
| Work Package: | WP4 |
| Lead beneficiary: | CRS4 |
| Contributing partners: | none |
| Dissemination level: | PU |

# History of changes

| Version | Changes | | Drafting | Review | Approval |
|---|---|---|---|---|---|
| 1 | -- | Signature | | | |
| | | Name | Vincent Moreau (CRS4) (Main author) | Ivan Di Piazza (ENEA) (WP Leader) | Giacomo Grasso (ENEA) (Coordinator) |
| | | Date | 07/07/2023 | 10/07/2023 | 12/07/2023 |
| | | Signature | | | |
| | | Name | [Name Surname] (ORG) (Main author) | [Name Surname] (ORG) (WP Leader) | Giacomo Grasso (ENEA) (Coordinator) |
| | | Date | | | |

# Abstract

The aim of this document is to check whether the sloshing phenomena can be satisfactorily addressed by CFD simulations. The modelling approach needs to be compatible with the overall primary coolant simulation of pool-type GEN-IV HLM fast reactors such as ALFRED and MYRRHA.

In the introduction, we describe the basic phenomenology, its relation to safety, and our operating strategy.

The CFD modelling needs to be validated by comparison with experimental results. In the first part, we expose the rationales for the definition of an experimental campaign to be realized by VKI on the SHAKESPEARE platform. We justify the use of water in a cylindrical tank of diameter 60 cm also giving elements of dimensional analysis.

Second, we describe the sloshing modelling and its CFD implementation. The Realizable k-e model is used with recommended STARCCM+ sub-models and parameter settings. Convection and temporal discretization are second order. Adaptive refinement of the free-surface is contemplated. A method to obtain with high accuracy the height of the free-surface in coincidence with a line-probe is described. The parameters determining the tank displacement are explicated. Numerical measures aimed both at controlling and maintaining the free-surface integrity are also described.

An experimental test by VKI is used for comparison is used to refine, adapt and validate the CFD modelling, leading to abandon the turbulent setting in favor of the laminar one. The experimental abrupt transition from the planar to the chaotic mode is reproduced with high precision by the CFD simulation. It is found out that the transition does not take place where expected from literature. For different forcing amplitudes, new frequency transition values are numerically determined and if later proved correct experimentally will demonstrate the capability of CFD to capture the essential sloshing phenomena.

# Table of contents

# 1 Introduction

This document is addressing the second argument in the objectives of WP4 as quoted below:

"(ii) To further enhance the modelling and computational readiness level of sloshing dynamics in compact liquid-metal filled pools and to retrieve the expected impact forces and dislocations on the involved components for a reference system (e.g. ALFRED)".

## 1.1 Basic phenomenology

Sloshing is the phenomena appearing when a tank partially filled with a liquid with a free-surface is "agitated": the free-surface acquires momentum and deforms in a variety of time dependent ways.

Usually when a tank is partially filled with a liquid, the liquid settles at the bottom of the tank due to the gravity force. If the tank is displaced or rotated, it applies an acceleration to external border of the fluid. The fluid inside will adapt to the tank acceleration by building an internal pressure gradient that is then transformed in motion of the fluid. Only in rare cases, the fluid motion, governed by the equations of the fluid-dynamics will coincide with the tank motion. In general, the fluid will exhibit a motion relatively to the tank reference frame, inducing and comprising a deformation of its free-surface. If the forcing has a strong periodic component near the natural frequencies of the tank then a coupling can appear and lead to a liquid displacement much higher than the forcing amplitude. In this case, the force exerted by the fluid on the tank can endanger the structural integrity of the tank and its supporting structure or even the stability of the vehicle holding the tank.

## 1.2 Relation to safety

Historically, sloshing induces a safety hazard in the transport of most if not all fluids. When the container is open, sloshing can make the fluid spill over, make people get dirty or be lost and contaminate the environment. When the container is closed, like in car reservoir, but more critically, in a tanker-truck or a super-tanker, sloshing can compromise the stability of the vector. In aeronautics and "rocket" science, the situation is even more critical as the accelerations can largely overcome the stability induced by gravity.

In this context, sloshing has been intensively and extensively investigated, bringing a large mole of available material and technical-scientific understanding. This is a good basis, even if our concern lays in a quite different framework.

What we want to evaluate is the effective possibility that sloshing can impact the resilience of the ALFRED main Vessel and internal components to seismic forcing.

## 1.3 Operative strategy

The design of ALFRED must take into account the possible effects of sloshing under seismic load. It is unrealistic to build a full scale model of ALFRED and put it on a shaking table to verify by trial

and error that everything goes safely and tests variants until a satisfying configuration is found. A more articulated and progressive approach is required.

First, we must understand the basics of the phenomena, the underlying physics and the controlling parameters. This can be done through literature review.

We must interpret this preliminary knowledge in terms useful to define a preliminary experimental campaign, compatibly with a series of constraints:

- the capabilities of the SHAKESPEARE shaking table operation;
- the possibility to make available a sound instrumentation;
- the possibility to numerically replicate the experimental campaign by mean of our CFD tools;
- the possibility to compare meaningful experimental measures with numerical result, hopefully allowing to validate these later;
- the possibility to proceed naturally towards further experimental campaigns progressively more obviously related to the seismic forcing of ALFRED.

In parallel, we must ensure the capability of our CFD instruments to replicate the experimental campaign and develop the necessary tools to make the CFD related constraints on the experiment essentially irrelevant. In other terms, the CFD tool must demonstrate sufficient versatility such that it allows comparison with whatever experimental data may come out.

# 2 Rationales for the experimental campaign definition

The rationales behind the definition of the first experimental campaign come from the integration of several considerations and analysis that are exposed in this part.

## 2.1 Liquid choice

We explain here briefly why water is a good choice for our experimental campaign, keeping in mind later check with mercury.

- Lead or LBE. Ideally, the fluid should be Lead or LBE. However, they cannot be used in this framework because they are not liquid at room temperature and it is way too costly to build a “hot” sloshing experimental setup.
- Mercury. The only heavy metal liquid at room temperature and relatively easy to purchase in sufficient quantities. It is very heavy and opaque. Its specific weight limits the volume operable. Its opacity limits the instrumentation. Use of mercury is subject to health safety concern.
- Water. Unlimited availability without particular safety concern. Low density allows larger volume and more easy and precise instrumentation. However, the density being much different from the Lead one, we must demonstrate why this is not an issue. Transparency allows more instrumentation options.

Dimensional analysis will show that in the present framework water can be representative of Lead or LBE upon applying the correct scaling. The main experimental campaign should be performed with the larger amount of water that can be easily handled and stored on the shaking table. Reduced scale experiments with mercury can be performed later on to demonstrate a posteriori the correctness of the dimensional analysis. This must be performed at the latest stages of the work program, at a time when the features to be scaled and reproduced are well understood.

## 2.2 Experimental focus and vessel rationales

Driven by the simplicity requirement and also a rapid literature survey, see [1],[2] and their references, we chose to have a cylindrical tank partially filled with tap water and make it subject to periodic unidimensional horizontal solicitation. We know from the literature survey the diagram frequency-amplitude solicitation diagram and its regions of interest to demonstrate experimental control and validate the numerical representation.

When the cylindrical tank water filling height is at least 1.5 times its radius, then the inviscid theory tells us that the effect of the bottom becomes negligible. The shaking table must allow this factor 1.5. Lower filling can still be foreseen at a later stage to inquire on more shallow configurations.

The larger transparent (Plexiglas) cylindrical vessel easily purchasable, that can be operated by the table with 1.5 radius water filling, has a diameter of ~60 cm.

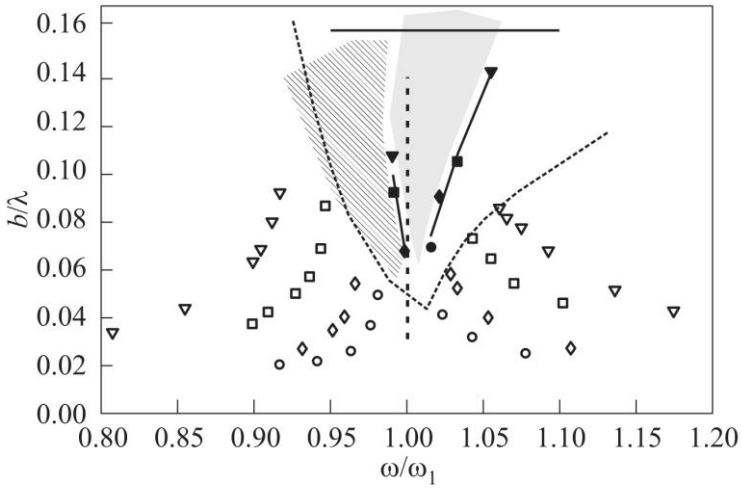


**Figure 1. From [1]. Amplitude-frequency diagram for four different forcing amplitudes $A_f/R$: ▽, planar wave mode 1; ▼, swirling wave mode for $A_f/R$ = 0.0266; ■ □, $A_f/R$ = 0.0133; ◆, ◇, $A_f/R$ = 0.0066; ◦, •, $A_f/R$ = 0.0033. A stable swirling wave (shaded region) exists between the filled symbols and chaos is observed to the left of it (hatched region). The dotted branches are the bounds of swirl of Abramson (ref. [4] in [1]). The upper horizontal line indicates $b\omega^2 = g$, giving $b/\lambda$ = 0.16 ($\lambda$ = 3.411 $R$). The tank, filled with water to $h/R$ ≈ 1.5, has a radius $R$ = 78 mm.**

## 2.3 Justification: elements of dimensional analysis

From the inviscid analysis of an infinite cylinder or radius $R$ partially filled with a liquid (and no cover gas), we obtain the first asymmetrical natural frequency formula for the free-surface. It

makes use of the important geometrical parameter $k_{11} = 1.841/R$. With this parameter, the simplified dispersion relation is:

$$\omega_{11}^2 = g k_{11}(1 + \sigma k_{11}^2/\rho\, g)$$

where $\omega_{11}$ is the first asymmetrical pulsation (in Rad/s), $g$ the gravity acceleration, $\rho$ the fluid density and $\sigma$ its surface tension.

Apparently, the natural frequency depends on the cylinder radius, gravity, fluid density and fluid surface tension. But density and surface tension only appear once and coupled in the form $\sigma/\rho$. Thus, the kinematic of the free-surface depends effectively on (1) only one fluid related property, the kinematic surface tension $\sigma/\rho$ (in $m^3/s^2$), (2) the cylinder radius and (3) the acceleration of gravity. As we do not intend to leave the earth surface, we can consider the gravity acceleration as a constant of our framework. The relative effect of the (kinematic) surface tension on the pulsation scales down with the square of the cylinder radius. So, the larger the radius, the less the effect of surface tension. This is quite in line with the common intuition. As our objective is to have valid extrapolations for ALFRED or MYRRHA whose vessel is essentially a cylinder several meters wide, surface tension is only a parasite of our experimental setup. This is an additional reason why we prefer to have the experimental vessel as large as possible.

Taking for granted that the surface tension effect can be made negligible, the dispersion relation simplifies to $\omega_0^2 = g k_{11} = 1.841\, g/R$. The natural frequency is higher for smaller cylinders. Measure instruments have usually a finite precision and have therefore a better relative precision for larger radii and smaller frequency. This arguments comfort the choice of a large cylinder.

To get a better insight on the possible parasite effect of surface tension, some relevant quantities are given in Table 1 both for water and mercury. This is however related to perturbations according to the inviscid theory. For real liquids, the fluid sticks to the walls instead of being free to slide effortlessly. Without entering considerations on the attachment angle and its possible hysteresis, we make a simple evaluation of a possible induced perturbation.

First, let us consider the length $L$ at which effects of surface tension and gravity are similar, i.e. $\sigma/\rho\, L^2 = g$ or $L = (\sigma/\rho g)^{1/2}$. On a border of width $L$, all around the cylinder, surface tension is expected to matter. Now, let's see what is the proportion $P$ of the free-surface concerned:

$$P = 2\pi\ LR/\pi R^2 = 2L/R$$

For water at ambient temperature $L$ = 2.7 mm. This mean that for a tank radius of 7.8 cm like the one used in [1], deviation from the inviscid theory is likely to appear for about 7% of the free-surface. This effect is potentially much larger than the deviations of the natural frequency and in an optic of extrapolation to ALFRED and MYRRHA vessels, it justifies better the need for the largest cylinder affordable.

With regard to the 1.5 radius filling requirement, it is clear that it comes from the inviscid theory in the limit of small displacements. For large displacements, the vessel bottom "comes closer" to the free surface and the volumes that are displaced below the free-surface feel more strongly the limitations of available space. We will see that this constraint induces a dissymmetry, not present in the inviscid analysis, of the waves with regards to the mean free-surface horizontal plane. This is

not a real issue but rather a feature useful to measure so as to better check the numerical implementation.

**Table 1: perturbation effects of surface tension and natural frequency for different cylinder radii at ambient temperature.**

| | Water | Mercury |
|---|---|---|
| Density $\rho$ [kg/m$^3$] | 998 | 13,534 |
| Surface tension $\sigma$ [N/m] | 0.073 | 0.486 |
| $\sigma/\rho$ [m$^3$/s$^2$] | 7.3 E-5 | 3.6 E-5 |
| $\sigma k_{11}^2/\rho g$ [adim] | 25.2E-6/$R^2$ | 12.4E-6/$R^2$ |
| $\sigma k_{11}^2/\rho g$ [adim] $R$ = 1 cm | 0.252 | 0.124 |
| $\sigma k_{11}^2/\rho g$ [adim] $R$ = 7.8 cm | 0.0041 | 0.0020 |
| $\sigma k_{11}^2/\rho g$ [adim] $R$ = 30 cm | 0.00028 | 0.000138 |
| $\sigma k_{11}^2/\rho g$ [adim] $R$ = 1 m | 0.0000252 | 0.0000124 |
| $\omega_0 = (g k_{11})^{1/2}$ [Rad/s] | 4.25/$R^{1/2}$ | |
| $f_0 = \omega_0/2\pi$ [1/s] | 0.667/$R^{1/2}$ | |
| $f_0 = \omega_0/2\pi$, $R$ = 1 cm | 6.67 | |
| $f_0 = \omega_0/2\pi$, $R$ = 7.8 cm | 2.39 | |
| $f_0 = \omega_0/2\pi$, $R$ = 30 cm | 1.22 | |
| $f_0 = \omega_0/2\pi$, $R$ = 1 m | 0.667 | |
| $\omega_{11}/\omega_0 - 1$ [adim] | (1+25.2E-6/$R^2$)$^{1/2}$-1 | (1+12.4E-6/$R^2$)$^{1/2}$-1 |
| $\omega_{11}/\omega_0 - 1$ [adim] $R$ = 1 cm | 0.119 | 0.060 |
| $\omega_{11}/\omega_0 - 1$ [adim] $R$ = 7.8 cm | 0.0021 | 0.0010 |
| $\omega_{11}/\omega_0 - 1$ [adim] $R$ = 30 cm | 0.00014 | 0.000069 |
| $\omega_{11}/\omega_0 - 1$ [adim] $R$ = 1 m | 1.3E-5 | 6.2E-6 |

# 3 Sloshing Modeling and CFD implementation

The first experimental campaign investigate the behavior of water filling for 45 cm height a cylindrical vessel with flat bottom or radius 30 cm. The vessel is positioned on and fixed to the SHAKESPEARE seismic platform which will impose periodic horizontal displacements of various intensities but below the centimeter range at a main frequency in the vicinity of the first asymmetric resonance.

The maximum free surface height is monitored as well as the free-surface height at a few horizontal positions.

Modelling of sloshing in view of its CFD implementation requires to comply a priori with several feature requirements:

- acceptable requirement of computational resources;
- compatibility with extension to the general ALFRED-MYRRHA CFD current modelling;
- easily adaptable to seismic input signals;
- fluid and (incompressible) flow independent;
- valid for laminar and turbulent flows;
- synergy and compatibility with the SHAKESPEARE seismic table.

## 3.1 Turbulence

The determination a priori of the turbulent character or not of the flow is aided by the determination of some Reynolds number: $\mathrm{Re} = UL/\nu$, where $U$ is a characteristic velocity, $L$ a characteristic length and $\nu$ the kinematic viscosity. Viscosity of water at ambient temperature is about $\nu = 10^{-6}$ m$^2$/s. It is common usage to take the hydraulic radius as characteristic length $R_h = D/4$ where $D$ is the cylinder diameter. In our case $R_h$ = 7.5 cm.

The characteristic velocity can be inferred from Figure 1. Remarking that for our vessel the y-axis gives approximately the height in meters, we expect sinusoidal waves of amplitude in the range 2-14 cm. The frequency is about $f_0$ = 1.2 Hz and the pulsation about $\omega_0$ = 8 /s giving a maximum velocity when the free-surface is flat between 0.16 and 1.1 m/s. As a result $\mathrm{Re}$ > 12,000, a clear indication that the flow is turbulent or should soon become turbulent if it starts at rest.

So, until proof of contrary, the flow is expected turbulent and modelled as such. This has been the case for the first 18-24 month of the project, until controlled experimental result were shared and could be compared with the numerical results. The matching was absolutely not satisfying. In the meantime, VKI made also simulations but considering a laminar flow and had excellent matching, indicating with very little doubt and against any a priori expectation that the flow is indeed laminar.

Laminar flows are generally more easy to handle than turbulent flows, especially free-surface flows. Issues like mass conservation, stability, and spurious currents do not arise so critically.

While useless for the first experimental campaign, the determination of a suitable setting for turbulent free-surface flows may reveal useful for extrapolation to much wider domains related to ALFRED or MYRRHA in which the Reynolds number can be one or two orders of magnitude higher. Besides, some settings are independent of the turbulent nature of the flow.

In the following, we will describe the turbulent setting that as been built.

## 3.2 Turbulence Settings

Simulations performed under the turbulent setting are using the RANS averaged Realizable k-ε model with ALL y+ boundary layer. Unless otherwise précised, STARCCM+ default setting are used. Convection and time discretization are second order.

## 3.3 Dynamical refinement

From version 17 of STARCCM+ (installed in 2022), it is now possible to dynamically refine the computational grid in vicinity of the free-surface and reset it when the free-surface moves away. This feature is particularly interesting in our case because the free-surface displacement encompass a very large part of the computational domain for which a permanent refined state is costly. In other words, this dynamical refinement allows a better free-surface capture at parity of global number of control volumes.

The dynamical refinement has been widely used during the preparatory phase. It seems very well adapted for some contexts, mainly open flows. In our case, we need very clean and precise results. Remeshing takes time so it must not be performed at each time step. It is suggested to remesh

every 5 time steps or so. We notice burst of pressure and maximum velocity after each remeshing, which are mostly absorbed during the next 4 time steps before the next remeshing starts. After other issues have been solved, one level of refinement works pretty well while with two levels of refinements, some small instabilities order 1 cm/s appear in the velocity field.

## 3.4 Case control

During the preparatory phase, there has been a progressive increase in the use of global parameters to control the simulation only at a top level without modifying directly field functions.

A typical simulation requires to define and is completely controlled by the following parameters:

- time laps of flow at rest (without forcing);
- asymptotic forcing amplitude;
- asymptotic forcing frequency as a multiple of the natural frequency;
- number of periods to reach the asymptotic amplitude;
- number of periods of steady periodic forcing;
- number of periods to get back to zero forcing.

## 3.5 Measures

There are basically two types of measurements that are performed on the simulation:

- the measurements that can be compared with the experimental one;
- the measurements that serve to check that the simulation is performing correctly.

This part deals with the first king of measurements.

The experiment is measuring:

1. the maximum free-surface height from post processing of images from a video of the experiment;
2. the free-surface position in correspondence with four vertical line probes located near the cylinder wall symmetrically on the reference axis with one axe collinear to the forcing;
3. the displacement of the vessel as a control of the displacement input;
4. free-surface integrity.

The corresponding numerical measures are obtained by use of parts, field functions, reports, monitors and plots.

The parts are primarily the geometrical constituent of the computational grid, mainly the volumes, their interfaces and their boundaries. Many types of derived parts can be built from these constituents, making use of geometrical and physical considerations. Points, lines, line probes, iso-surfaces of physical quantities, cell sets and streamlines are among the more common examples.

The field functions allow to recover all and any field that can be built from existing fields such as velocity, volume fraction, density, pressure, temperature, viscosity, turbulent energy and so on. Many fields are built-in and directly accessible, other fields can be built from them by use of field functions.

The reports can access all field functions separately on whatever relevant group of parts and can return indicator such as minimum, maximum, average, sum or integral value of the field function.

The monitors register the value returned by the reports on an iteration or time-step or time interval basis. The data can be further assembled in plot representations.

We are now in condition to explain how the experimental measures can be replicated numerically.

### 3.5.1 Maximum free-surface height

A derived part is constructed in the form of the iso-surface of the water volume fraction, at value 0.5, over the entire fluid domain. A report takes the maximum value of the height over this iso-surface and is registered by a monitor and assembled in a dedicated plot.

### 3.5.2 Free-surface at vertical line probes

The numerical representation initially implemented was not totally satisfying and a different, better one, had to be found out.

#### *3.5.2.1 First representation*

For each experimental line probe, a corresponding vertical line probe as been constructed. It consists in a series of points separated by a constant interval. A derived part is defined by taking only the points for which the water volume fraction is above 0.5. Then a report returns the maximum height value on this derived part.

The volume fraction in each point is in fact the value given to the control volume it falls into. If more than one point lies in the same control volume, they all share the same volume fraction value. This means that the precision of the measure is strongly limited by the control volume vertical size. At first glance, this approach seems optimum. An illustration is given below.

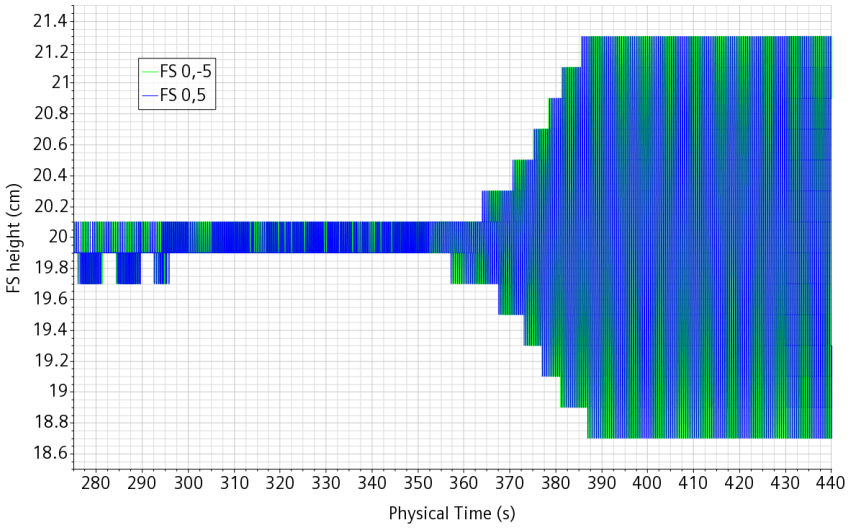


**Figure 2. Example of the time history of the position of the free-surface at a vertical probe.**

#### 3.5.2.2 Second and final representation

Remarking that the signal given by the maximum free-surface height was way much smoother and precise that the one on the vertical lines, we inquired on a way to obtain the same signal quality.

The overall free-surface derived part already being available, new derived parts were defined by restricting the free-surface to a small surrounding of the line probe horizontal position. Then a report returns the surface averaged height on this surrounding. The surrounding is large enough only to always contain at list one cell of the free-surface part. If too small, the signal can be occasionally lost. If too large, it can be smeared. The surrounding depends on the computational grid and must be checked each time this later is changed. However, the final signal is extremely smooth and able to report periodic oscillations at the micron size with control volumes in the millimeter range. This is useful to determine accurately the numerical natural frequency and its decay characteristics.

In Figure 3, we show the free-surface height at the four measured positions in a case let settled for quite a long time, until no residual periodic oscillation could be clearly identified. The signal is very smooth, especially considering that the vertical scale span a range of 0.2 µm.

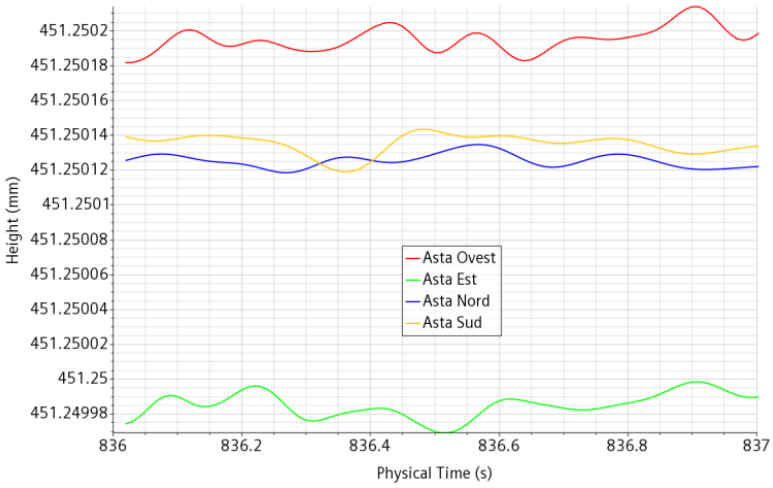


**Figure 3. Height of the free-surface at four position in a 1 s time lap.**

### 3.5.3 Displacement

The displacement being oriented along the x-axis, a report returns the maximum x-coordinate over the vessel bottom. It is stored in a dedicated monitor from which it can be plotted. This kind of report is operated only on an existing small part to avoid useless calculations. The signal is also easy to further scale and translate at the plot stage.

Similarly to the experiment, the displacement is imposed by setting either a displacement or a velocity law. It is however measured a posteriori for consistency check.

### 3.5.4 Free-surface integrity

Thanks to the transparency of the medium and of the vessel, it can be controlled visually that there is no relevant occurrence of bubble inclusion or droplets ejections. In fact, in this first

experimental campaign, we want to explore the space of parameters in which this feature remains true.

Numerically, thinks can easily become tricky. It is very easy that the free-surface become smeared or that blobs of low air volume fraction unphysically wander into the water, slowly developing end finally jeopardizing the simulation. It is very easy to stay unaware of such phenomena until it is too late because if the air volume fraction is below a few percent, then it is not individuated by a usual color map spanning the volume fraction from 0 to 100%.

To get rid of the phenomena, one must first be able to observe it the sooner the better.

Pollution of one phase into the other can be monitored by creating (dynamical) cell sets containing all the control volumes for which the volume faction is very low but not irrelevant. By default, a volume fraction of any phase is bounded low at $10^{-10}$ for stability or the simulation. So, except occasionally at the free-surface, a volume fraction in the range $[10^{-8}; 10^{-3}]$ or so is indication of spurious inclusion in the other phase.

The volume of such cell sets is then monitored. As said before, due to the free-surface, it cannot be null. But monitoring allows to capture an anomalous increase of the phenomena. On a more qualitative point of view an accurate choice of volume fraction range allows to pinpoint the phenomena on classical representation scenes. This is illustrated in Figure 4, hereafter.

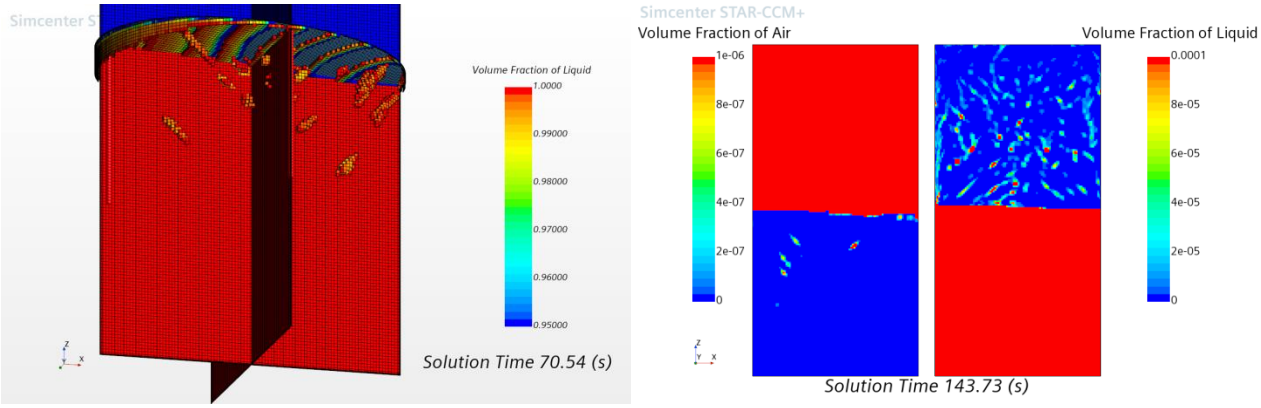


**Figure 4. Illustrations of methods to observe and monitor anomalous phase inclusions.**

## 3.6 Further numerical control and measures

While the number of experimental measures is by force limited, this is much less true for numerical measures. Because there cannot be direct comparison, further numerical measure cannot really serve to validate the simulation. Instead, they can serve to:

- check the internal simulation consistency;
- infer possible flow features that cannot be measured;
- provide input for future experimental measurements.

We now expand the argument with some illustrative examples.

### 3.6.1 Wall pressure measurements

Sloshing induces a variable pressure load on the vessel. This load can be numerically reported by integrating the product pressure per normal vector over the entire vessel wall. Once again, the pressure components can be shifted and rescaled at plotting time, for example by removing the vertical component of the pressure load at rest.

As pressure gauge measurements on the walls are expected at a later stage, it is useful to start checking the effective numerical availability.

While not tested here, if necessary, also torque similar numerical measurements can be performed.

### 3.6.2 Velocity check

The velocity field is readily available from the simulation in every point of the computational domain. Spurious velocities on or near the free-surface are a widely known candidate for unphysical behavior of the free-surface. In fact, an initial difficult task is to stabilize a simulation with an initial free-surface and the fluids (almost) completely at rest. It is therefore useful to monitor the maximum velocity in time in the computational domain. This is not sufficient because is case of spurious velocities, it is also useful to know where they appear. This is done in two complementary steps.

First the overall maximum velocity is monitored, but also the maximum velocity weighted by each of the two volume fractions and finally the maximum velocity restricted to the free-surface derived part. So, in case a spurious velocity appears as indicated by the first monitor, we can infer from the other ones whether is appears in the water, in the air or at the free-surface. If neither of the last three monitors indicate a spurious velocity, it means the this later appears in the immediate vicinity of the free surface but not exactly on it.

The secondary step consists in building a dynamical cell set with all computational volumes showing a velocity above a certain threshold which must be determined on a case by case basis.

The first step is partially illustrated in Figure 5 where we can see the maximum velocity in the water (in green) gently following the sloshing oscillation while unphysical burst of velocities (in red) appear globally and thus somewhere above the free-surface. In this particular case, different behaviors can be seen as the result of partially failed attempts to solve the issue by changes in the numerical setting.

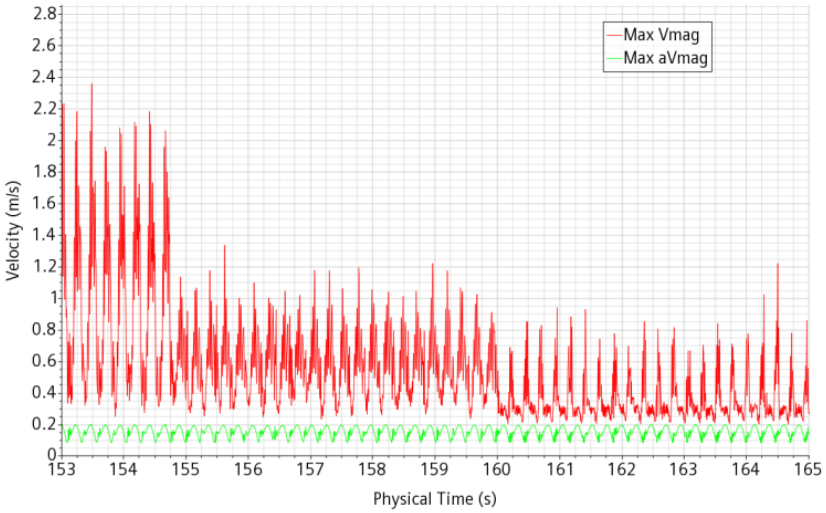


Figure 5. Partial history of a maximum velocity monitor and a maximum water volume fraction weighted velocity monitor.

### 3.6.3 Mass conservation and spurious phase diffusion.

A known issue in the simulation of multiphase flows is the frequent occurrence of mass loss or mass gain. In open domains, usually nobody cares because the gain or loss is small and the residence time is limited so that there cannot be accumulation in time. The issue is much more critical for closed domains subject to long transient flows. In effect, a small mass gain in time can accumulate up to the point that the volume occupied by the phase is macroscopically increasing, for example leading to a slow drift in the mean height of a free-surface. From preliminary simulation, we expect that asymptotic behaviors can be reached only after several hundreds of forcing periods, which puts us in this later case.

It is therefore necessary to monitor in time the inventory of each phase. This is done by a report returning the integral of the volume fraction over the whole computational domain. It is often difficult to know why there is a mass drift and how to remove the cause. In some case, we have do get along with it and make artificial corrections. The method for the correction is the following:

1. measure the mass error of one phase;
2. localize a “quiet” region where the phase volume fraction is unit;
3. set a volume fraction source term in this region, proportional to the mass error and divided by a characteristic time suitably dimensioned;
4. perform steps 2 and 3 for the other phase in such a way to avoid overall creation of volume.

Creation of volume in a closed domain is physically inconsistent. Numerically this is resolved by bad convergence of the pressure correction which in turn tends to concentrate the error and brings the appearance of local possibly high spurious velocities. One thus must be very cautious playing with volume fraction sources in closed domains.

As mentioned before, the minimum volume fraction of a phase is bounded below to $10^{-10}$ for numerical stability reasons. The exponent can be modified at the risk of the user and we will not explore this possibility here. So, there is always at least a tiny seed for the phases. Various phenomena can bring the simulation locally into a state where the sum of the volume fraction is

not exactly unit. The way the software resolve the situation is by applying a pressure correction and/or renormalize in some way the volume fractions. Details are complex and not completely known. Fact is that the very dispersed phase often tends to see its volume fraction grow and this growth seem to be quite exponential at the beginning, meaning that the growth rate is proportional to the current volume fraction. This also means that if the phenomena is contrasted at its very beginning then the cure can be extremely light and have whatsoever no measurable impact on the quality of the simulation.

The cure is performed as follows:

1. an air volume fraction sink is defined and applied in the water region. The term is proportional to the air volume fraction and the coefficient of proportionality is representative of a carefully set characteristic time. To localize the sink term in the water region, it is multiplied by the water volume fraction;
2. the integral of the sink term is monitored;
3. an equivalent source term is applied in a “quiet” air region;
4. steps 1 to 3 are replicated for water.

In the end the source/sink terms in the “quiet” region are the sum of two contributions, one aimed at preserving the overall phase inventory and the other the compensate the cleaning of the phase in the other phase domain.

The characteristic times are stored as parameters so as to be easily changed without modifying the writing of the user functions.

An extreme care must be taken to ensure that the global volume balance is at null sum. In particular, it is not enough that the null sum is reach only at a single precision level. Here we explain how a very slight error contributed to an extremely large quantity of trouble.

The target volume inventory of each phase is measured at the simulation initialization or is calculated analytically. Same thing for the total volume of the computational domain. The total volume is stored as a parameter.

Once the target water volume is decided, to be cautious, the target air volume is defined by difference with the total volume and both are stored as parameters. Except that the total volume is neither exactly the analytical volume nor the volume given (in single precision) by the report in the output window of the software. There is a small imbalance because the source terms objective was to fill a slightly different volume than available.

To solve the issue a report is built as the difference between the former report and its single value precision value. From the difference, the total volume could be adjusted to a sufficiently higher number of digits. This correction greatly contributed to remove the spurious velocity issue.

# 4 Numerical model

## 4.1 Historic

A very large number of simulation as been performed in order both to help determine the experimental setting and also to find a satisfying numerical setting. Truth is that the simulations have been plagued for a very long time with excessive bursts of spurious velocities near the walls or close to the free surface or randomly appearing in the air bulk. Until the very precisely controlled experimental result from VKI were available, the aim was to have “clean” simulation with plausible results. By clean, we mean simulations without unphysical bursts of velocity and without mutual pollution of the phases. The process to get clean simulation has been long and non-linear and brought us to stick to some empirical but necessary consideration:

- the temporal discretization must be set second order;
- the pressure under-relaxation factor must be raised from the multi-phase default 0.2 up to 0.4 or 0.5 (it is still not clear which is better);
- the velocity under-relaxation factor must be set to 0.7;
- strong refinement at the wall, maybe in conjunction with high cell aspect ratio, conflicts with the surface tension treatment. Happened only for small vessels (7.8 cm radius) and water;
- volumetric source terms are both necessary and must be handled very carefully and precisely.

The more surprising requirement is on the pressure under-relaxation factor. It must be understood under the condition of 5 iteration per time step and CFL controlled time step. Usually, in situation when numerical convergence is at risk, it is good practice to reduce the under relaxation factors. It is the contrary in our case. Our interpretation is that pressure is bound to adapt fast to variations of the free surface. In particular the pressure gradient is very different both sides of the free-surface. If pressure adaptation lags, then spurious velocities develop.

In Figure 6, we show on a non-better described sloshing test case what happens to the spurious maximum velocity in red when correction actions are taken. On the left, we see the effect of raising the pressure under-relaxation factor from 0.2 to 0.5 at time 65 s. Apart from the sudden drop at time 65 s, we also see a slow rising instability however at a much lower intensity. The full time of the simulation is shown on the right. The disappearance of the residual flow instability at time about 115 s is due to the improved handling of the volume fraction source terms.

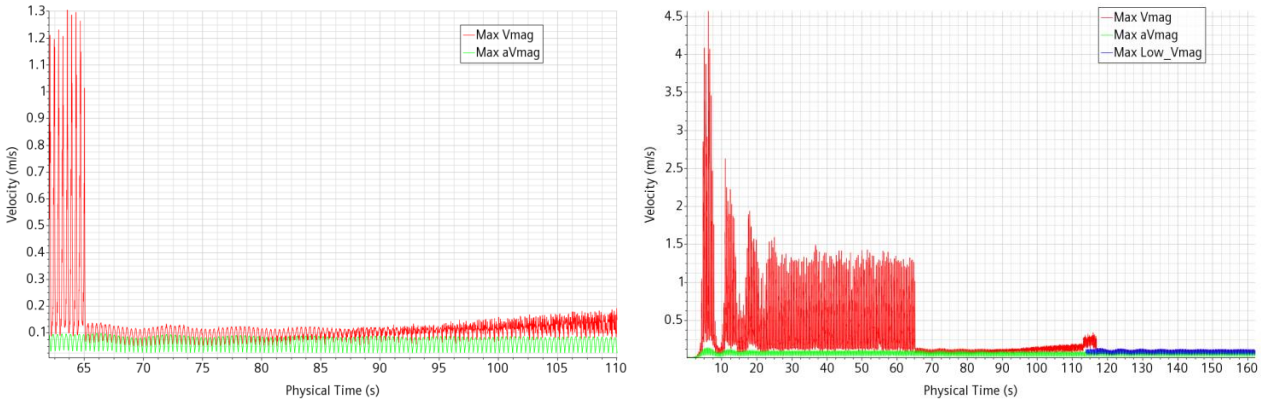


**Figure 6. Time history of the maximum velocity in a test case in which the spurious velocity has finally been vanquished.**

## 4.2 Experimental reference configuration

The VKI experiment is performed on a vertical cylinder of internal radius $R$ = 29.9 cm and flat bottom. It is filled with tap water up to 1.5 $R$.

The first experimental tests results have been illustrated by VKI at mid September 2022. Then, the post processing and sharing of some of the tests results followed. In particular, three tests have been shared:

- 92% natural frequency (linear test);
- 92.55% (near transition);
- 92.75% (transition).

The exact geometry of the test section was provided and the input conditions. The table X-displacement in time (time step 0.01 s) was provided both as input to the table and as measured experimentally by laser. The heights of the free surface level at four positions were provided as tests results, still at 100 Hz.

The numerical geometry has been updated to reflect the experimental one. In particular, the vertical probes have been positioned at 5 cm of the vessel wall.

The precise value of the natural pulsation under the inviscid linear theory is $\omega_{11}$ = 7.77 rad/s corresponding to the frequency $f_{11}$ = 1.236 Hz.

## 4.3 Numerical setup

Here are the main numerical setup for the simulation of the linear test case 92% natural frequency and sinusoidal forcing with amplitude $A_f$ = 3.98 mm. This setup is built in the turbulence framework and later changes are indicated. When a setting is not indicated it is normally the default one:

- base mesh size = 0.02 m (for faster run). Later on, the mesh was refined (1 cm);
- adaptive mesh with 1 or 2 refinement levels. Later on, with refined mesh and turbulent setting, the adaptive mesh was disabled;

- adaptive time-step: Convective & Free surface CFL condition (Default). Maximum time step: 0.01 s;
- iterations per time-step: 5;
- different turbulent regimes were tested: RANS Realizable K-ε and LES;
- also laminar regime was tested;
- convection 2$^{nd}$ order; time discretization: 2$^{nd}$ order;
- pressure under–relaxation factor: 0.5;
- velocity under-relaxation factor: 0.7.

For a consistent comparison, the VKI Table input (X-displacement ) was imported in STAR-CCM+ and used directly. Motion was defined as trajectory and displacement along trajectory through an imported table by linear interpolation with only X-displacement (hence, putting y = z = 0).

The simulation is initialized and stabilized for about 5 s. Initialization is performed as follows:

- the volume fractions are initialized as requires;
- time step is set to a very low value: $10^{-10}$ s and the automatic increase of time-step is bounded to 2. This allows the pressure to adapt without creating high initial spurious velocities;
- the time-step reaches is maximum value 0.01 s after about 25 time-steps;
- the displacement is initiated only after a few seconds to let possible small induced currents settle.

Comparison with the experiment is done on the evolution of the free-surface at two positions, on the reference coordinate axis X and Y. For the linear forcing the two remnant positions are redundant.

### 4.3.1 Comparison with the turbulent simulation.

The k- ε model is used with Two-Layer wall functions.

Comparison of the evolution of the free-surface position during the first 60 s of the test is shown on Figure 7. First a comment on the experimental result. The modulation of the signal is due to the interference of the forcing frequency with the natural frequency. The signal at the forcing frequency builds up very fast to a constant amplitude while the natural frequency signal is built up at the beginning and then shows a slow exponential decay. The overall shape of the curve and of its envelop furnish the framework of critical parameters that the simulation must correctly reproduce:

- the envelop first maximum (and minimum) amplitude;
- the time of this envelop first maximum (and minimum);
- the time of the interference first nodes;
- the envelop amplitude at these times;
- the decay rate between successive envelop maximums;
- the asymptotic amplitude.

From the figure, we can see verify that the correct forcing frequency has been set. We can also see that the initial growth of the envelop is well reproduced. For the rest, nothing goes satisfactorily: the envelop first maximum is higher and later, the first node is strongly delayed is much weaker and finally the asymptotic amplitude is reached much too soon and at a too high value.

All these defects points to an excess of the signal initial build up combined with a later excessive decay of the natural frequency part of the signal.

This means that, in spite of consolidated practice of a priori evaluation, the flow could still be laminar. This observation was already interiorized by our VKI colleagues and it is time for us to follow their lead and test laminar settings.

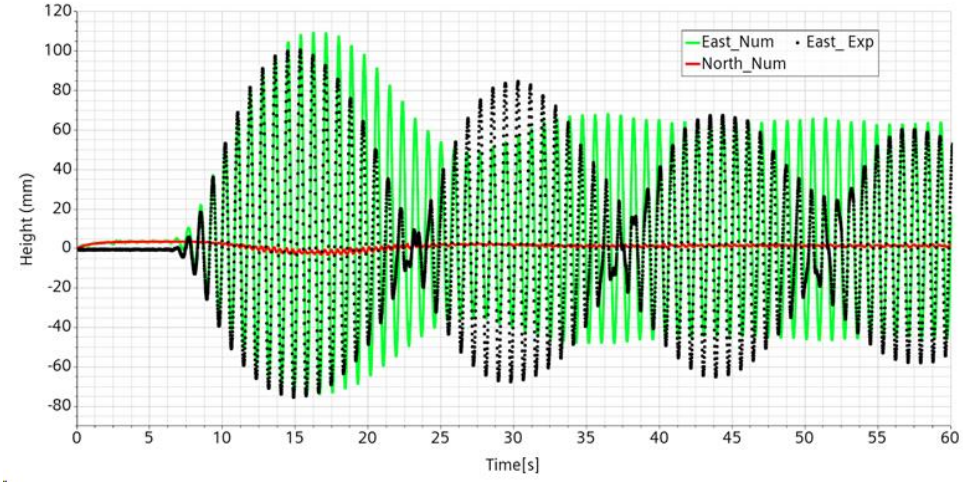


Figure 7. K-ε numerical (green) and experimental (Black) free surface height for East probe

## 4.3.2 Laminar simulations

In the following, we show the comparison of the experiment with laminar simulation. The first laminar simulation showed decisive improvement but was not yet satisfying. It allowed to inquire on secondary features of the experiment that were not well understood and implemented.

Switching from a turbulent simulation setting to a laminar one is straightforward in the STARCCM+ framework. One open the “select model” window, deactivate all turbulence related models and activate the laminar one. And that’s it.

### 4.3.2.1 Laminar simulation from direct setting change.

The result of the simulation is shown on Figure 8. The result is much better than before. In particular:

- the first envelop maximum is captured;
- the decay of the envelop successive maxima looks quite well;
- the envelop nodes are much more pronounced.

However, other features are still not satisfying:

- the first node is strongly retarded;
- the envelop minima do not behave too well.

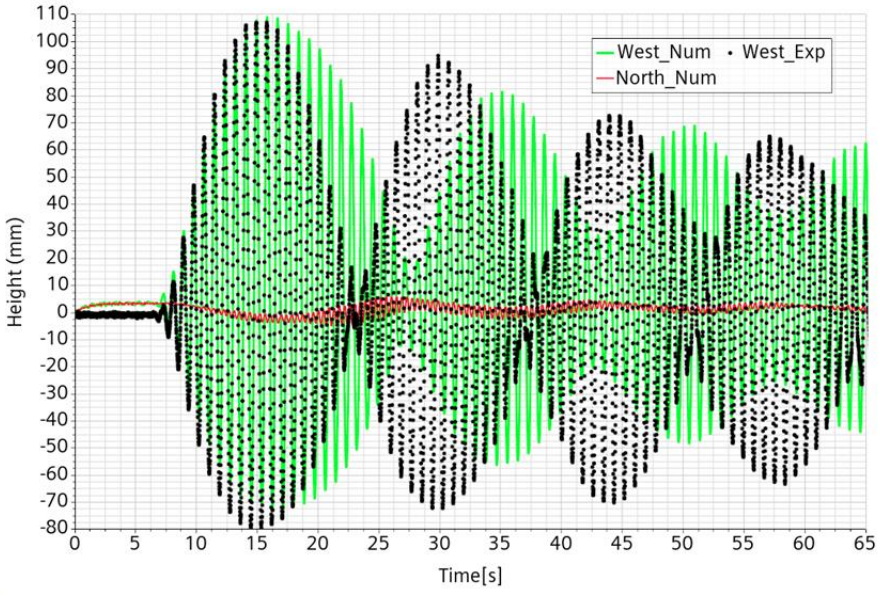


Figure 8. First laminar simulation.

The laminar approach seems definitively more adapted than the turbulent one.

#### 4.3.2.2 Simulation with suggested analytical forcing

The previous simulations have been performed using the measured displacement and a slight regularization of it. Some regularization was necessary because the small rumor in the displacement signal led by driving twice to an acceleration dominate by rumor.

As we suspect to introduce an additional uncertainty on the forcing rather than imposing the correct signal, we redo the simulation with the analytical forcing that has been initially suggested. We also take the occasion to adjust the curve origin. The free-surface height comparison experimental-numerical with suggested input displacement is shown in Figure 9. While there is still some discrepancy, the simulation results are now close to the experimental one with only a slight lag for the first envelop node. This lag appears at the beginning but do not increase for the later nodes. This means that the interference pattern is now correctly captured. The convergence towards the asymptotic cycle seems also reasonable.

All in all, this means that the analytical input signal is most probably much closer to the real one than the measured one.

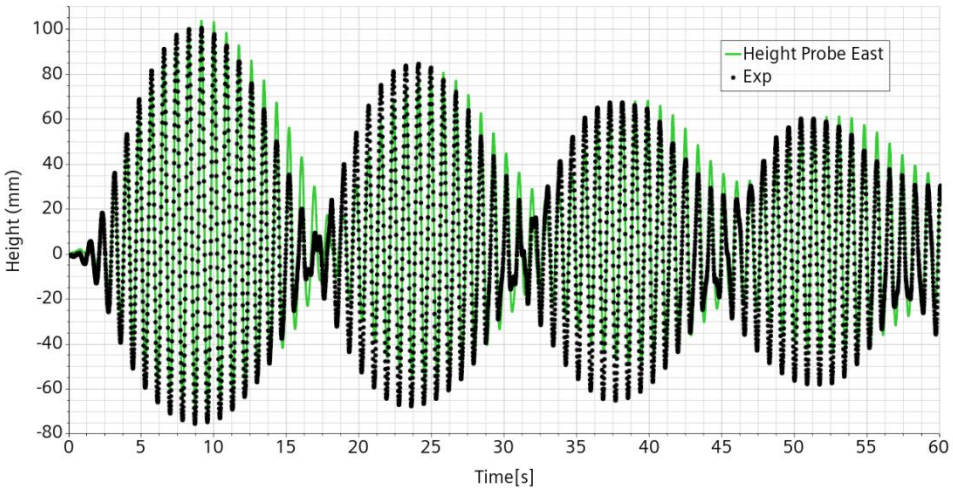


**Figure 9. Free-surface height comparison experimental-numerical with suggested input displacement.**

#### 4.3.2.3 Simulation with implemented numerical forcing.

In Figure 10, we compare three forcing signals: measured, suggested and implemented. As already mentioned, the measured signal lacks regularity and at the smaller scale even unrealistic close to the extremes. We also notice that the implemented signal, while identical to the suggested one after 3.5 s, is slightly different to it during the first 3 s. In the suggested signal, the envelop was controlled by squared sinus shape. But the implement input the square was omitted leading to a sharper and faster increase.

The simulation is redone therefore with the effective implemented input forcing signal. The result is shown in Figure 11. We can see that the rather small difference in the initial input signal has a non-negligible effect on the numerical results. In particular the discrepancy with the experimental results has been about halved.

There are several sources of uncertainty. From the experimental wide, we have: the real output signal, the exact position of the probe and the precision of the measure. From the numerical side, we have: mesh dependence, numerical scheme dependence, time step, etc. While we can still improve the numerical precision, the comparison with the experimental data is already so good that any further improvement maybe purely casual and not necessarily also related to a simulation improvement.

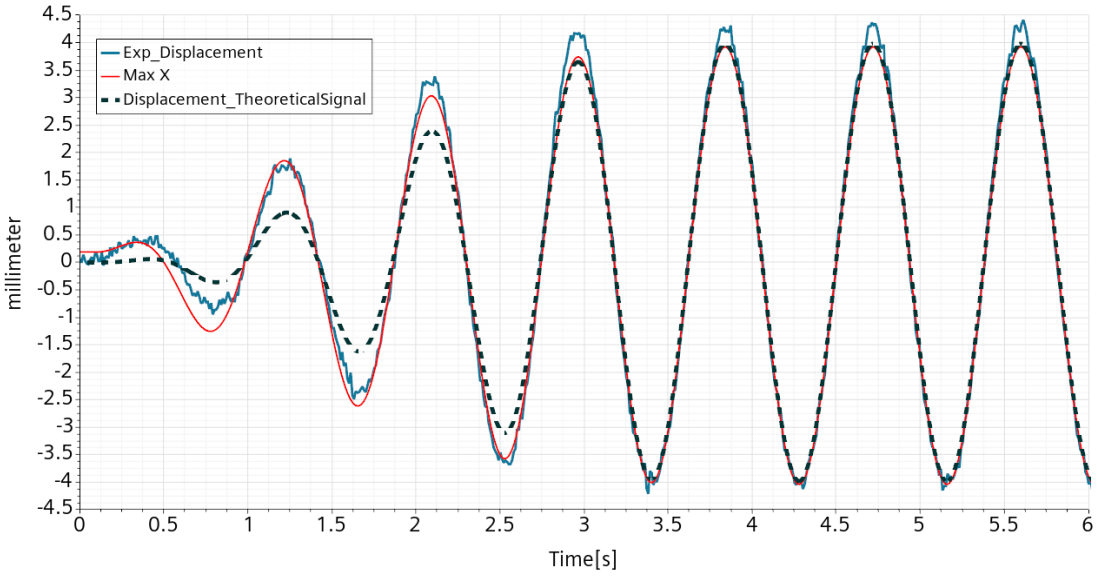


Figure 10. Comparison between the three input displacement signal: measured in blue, input in the table in red and initially suggested in dashed black.

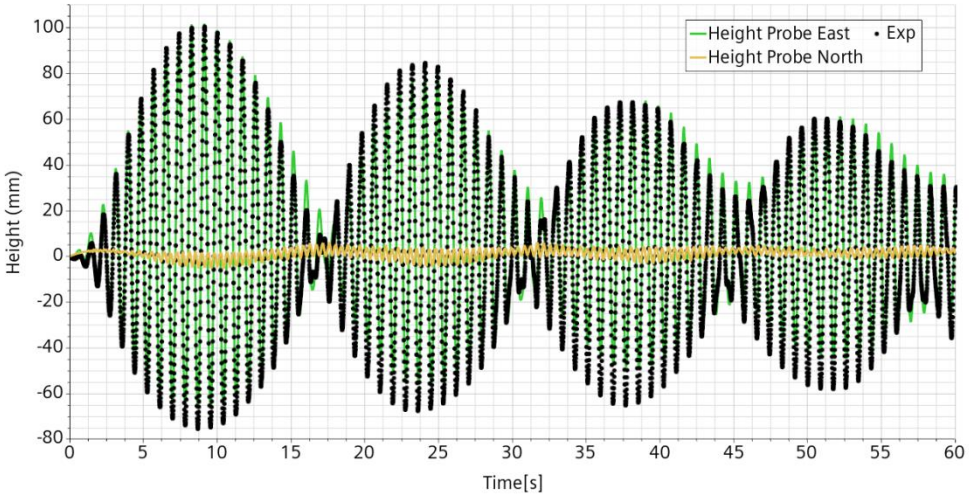


Figure 11. Free-surface height comparison experimental-numerical with implemented input displacement.

## 4.4 Physical setup dependency

The previous simulation has been reviewed and a few second order correction to the setting performed: residual initial Y-displacement removed, initial X-displacement set as velocity and further corrected. Also, included Surface Tension 0.072 N/m, Interface Artificial Viscosity 0.1 adim and Semi-implicit Surface Tension.

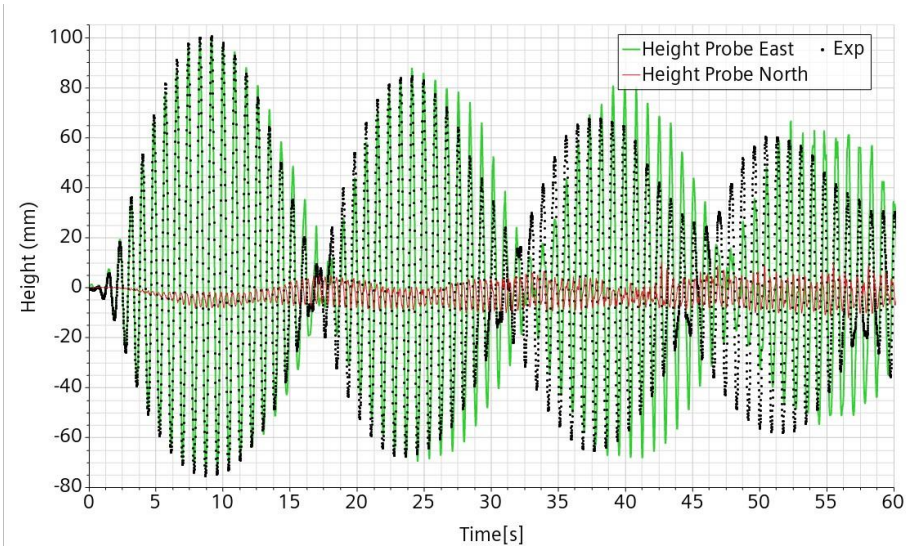


Figure 12. Probe East free-surface comparison with experiment. Reference case for perturbation analysis.

### 4.4.1 Initialization setup

Free-surface flows are always difficult to initialize. Here is how we did it this time.

- Set an initial volume fraction profile: center cells bellow 45 cm are Water, otherwise Air.
- Measure precisely the water volume. This number depends on the discretization and serves to have consistent volume fraction source terms.
- Set the initial pressure from a dedicated function consistently with the Water level.
- Set a 100 iteration ramp (regular timestep 0.002s, 5 iterations/timestep) for all solvers: velocity, pressure and volume fraction.
- Deactivate the displacement.
- Run for a few seconds. (Check flow is relatively quiet)
- Reset time/iterations.
- Reactivate the displacement.
- Run.

### 4.4.2 Reference case attempt

The reference case is run for 180 s. The comparison with the experiment is much worse than before. We are missing something.

In relation to the coming perturbation analysis, here are its parameters under scrutiny:

- signal amplitude: $A_f$ = 3.98 mm;
- temperature: 30 °C -> Water dynamic viscosity $\mu$ = 0.8E-3 Pa s;
- trimmed mesh: 1 cm top and bottom, 0.5 cm center. No Boundary Layer.

When the flow was thought to be turbulent and modelled as such, a check on the effect of temperature induced change of viscosity showed no visible effect. It is possible that with this low viscosity, there is a mild transition towards turbulence in time. In effect after a while the north numerical probe exhibits a small chaotic behavior, as shown in Figure 13.

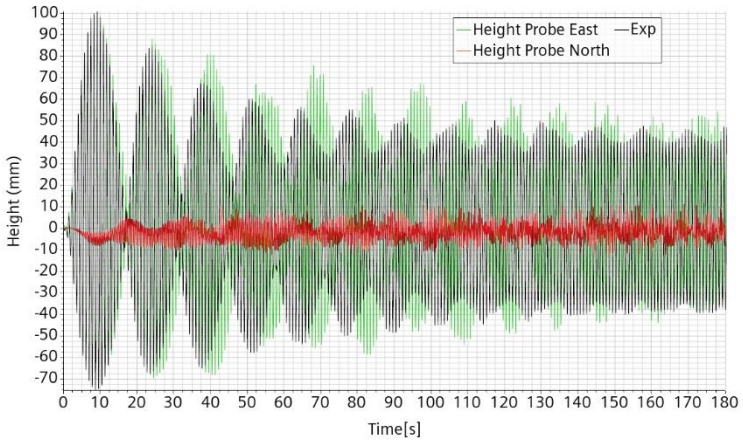


Figure 13. Trimmed mesh. Viscosity 0.8E-3 Pa s. Comparison numerical-experimental free surface height at East probe.

### 4.4.3 Perturbation analysis

Upon the hypothesis that the discrepancy could be due to physical reasons. We first redo the simulation increasing the viscosity to 1.3E-3 Pa s, as for water temperature of 10 °C. The result is almost identical during the first 60 s with a very small reduced lag.

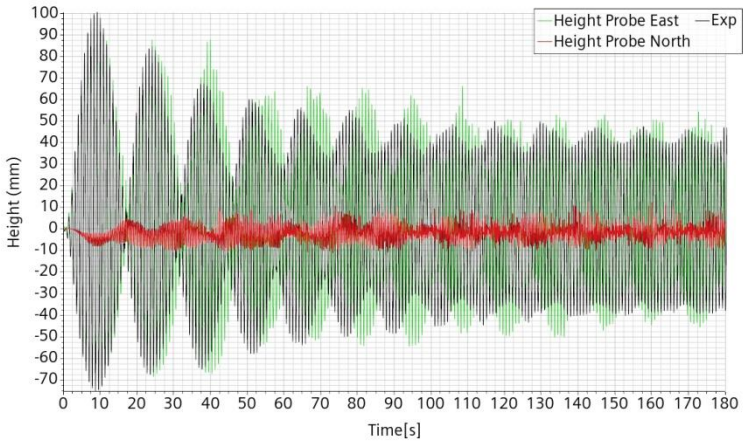


Figure 14. Trimmed mesh. Viscosity 1.3E-3 Pa s. Comparison numerical-experimental free surface height at East probe.

A new simulation with viscosity increased to 3.E-3 Pa s shows a much better improvement and a very good matching during the first 30 s. There is still a tiny lag though.

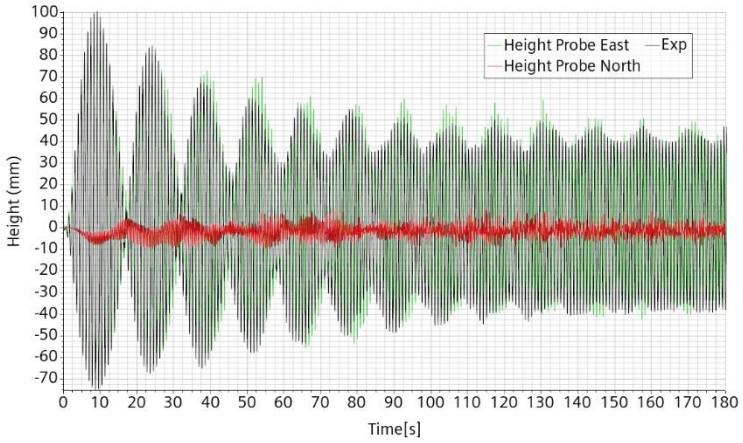


Figure 15. Trimmed mesh. Viscosity 3.E-3 Pa s. Comparison numerical-experimental free surface height at East probe.

Two hypotheses can be formulated:

- the experimental water was contaminated somehow and has a much higher viscosity;
- the energy transfer to the natural frequency relies mostly to the boundary layer correct capture and a numerical boundary layer must be added.

Moreover, a large numerical dissipation could also do the job.

A new simulation with a 3 cell BL of total size 2.5 mm is run, this time with a viscosity of 1.E-3 Pa s, as for a 20 °C temperature.

Results remain quite similar. But as it is more likely to have a temperature at 20 °C rather than at 30 °C, this case becomes the reference case.

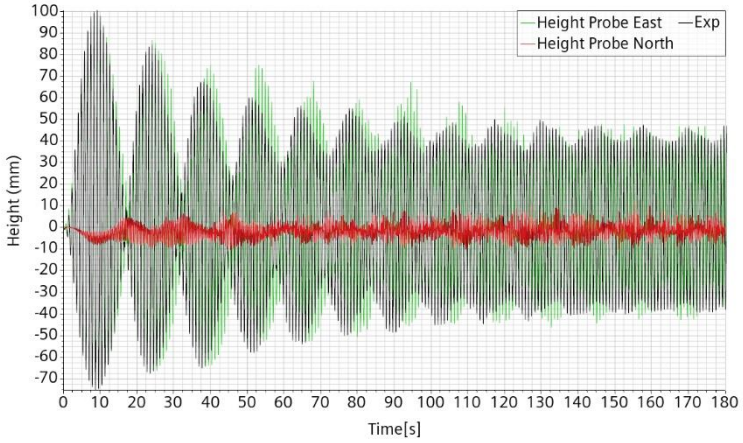


Figure 16. Trimmed mesh with BL. Viscosity 1.0E-3 Pa s. Comparison numerical-experimental free surface height at East probe.

## 4.5 Numerical setup dependency

Now that we have asserted that it is possible to reproduce correctly a simple sloshing case, we explore the space of numerical parameters allowing to keep this feature of even to improve it, taking into account the model complexity, the computational requirement and the extrapolation potentiality.

### 4.5.1 Adaptive mesh with two refinements level and time-step CFL controls.

The last reference case is rerun after including time step controls related to the CFL and to the free-surface, and also including two levels of adaptive mesh refinement, all with default parameters.

The result is indicated in Figure 17. We can see that now the first three modulations are almost perfectly captured in the direction of the forcing, with a first peak of 100 mm amplitude. Then, there is a progressive deviation but the modulation frequency is preserved. The numerical solution converges more slowly towards the limit cycle but seems to do so at a similar amplitude about 40 mm.

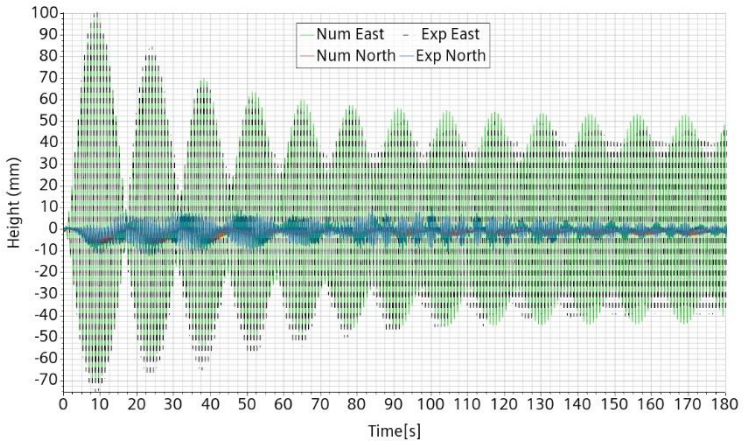


Figure 17. Reference case with two levels of adapted mesh and CFL control.

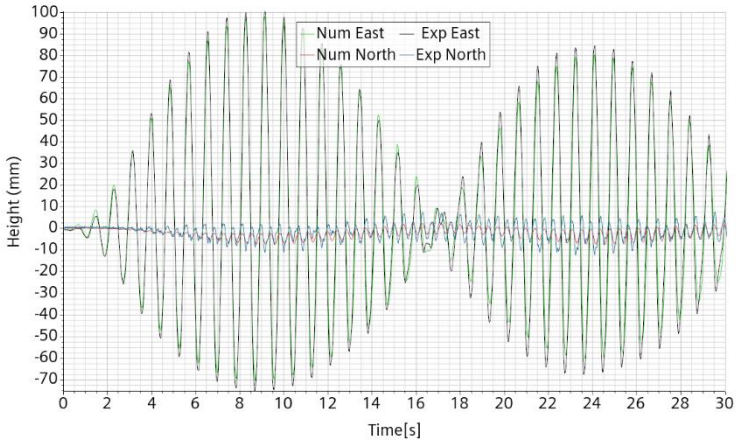


Figure 18. Reference case with two levels of adapted mesh and CFL control. First 30s and orthogonal displacement added.

### 4.5.2 Adaptive mesh with only one refinements level and time-step CFL controls.

The reference case is run with only one level of mesh refinement instead of two. The maximum amplitude at each modulation in now clearly below the experimental one. The modulation frequency remains correct. The limit cycle is approached faster but its amplitude is very close to

the experimental one. There is therefore a non-negligible effect of the free-surface refinement. The orthogonal numerical oscillation remains about half the experimental one. See Figure 19.

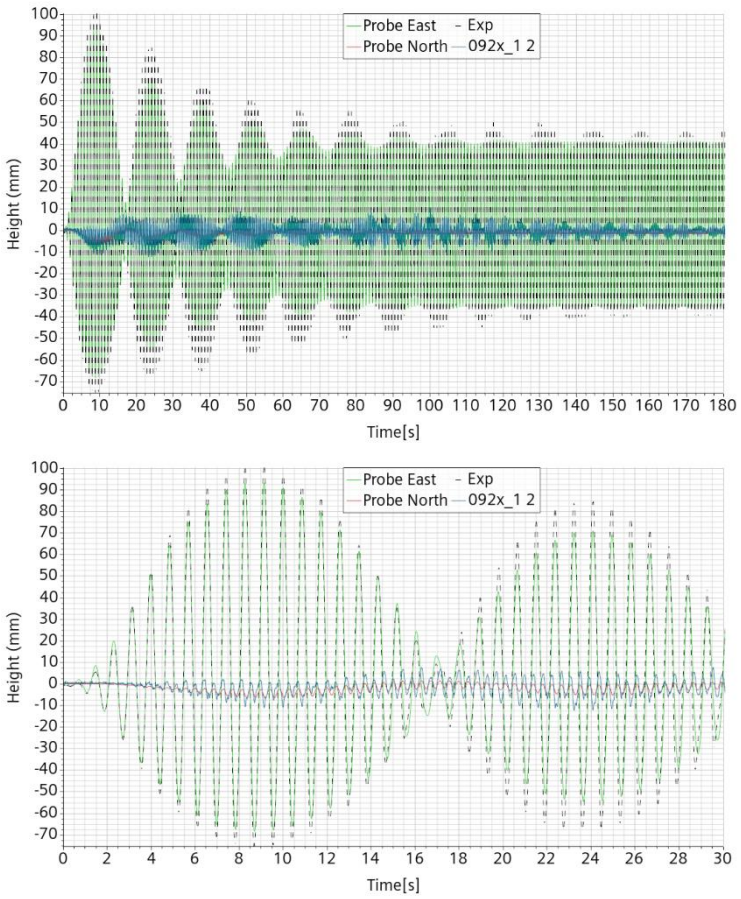


Figure 19. Reference case with only one levels of adaptive refinement.

### 4.5.3 Only time-step CFL controls

No adaptive refinement but still time-step controlled by CFL and free-surface speed. The irregularity of the local maximum indicates the appearance of some possible parasite waves. These are not present in the more refined simulations and are therefore likely to be purely of numerical nature.

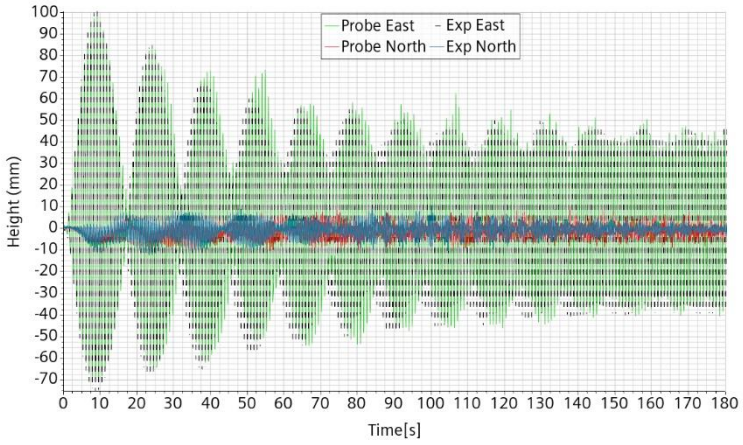

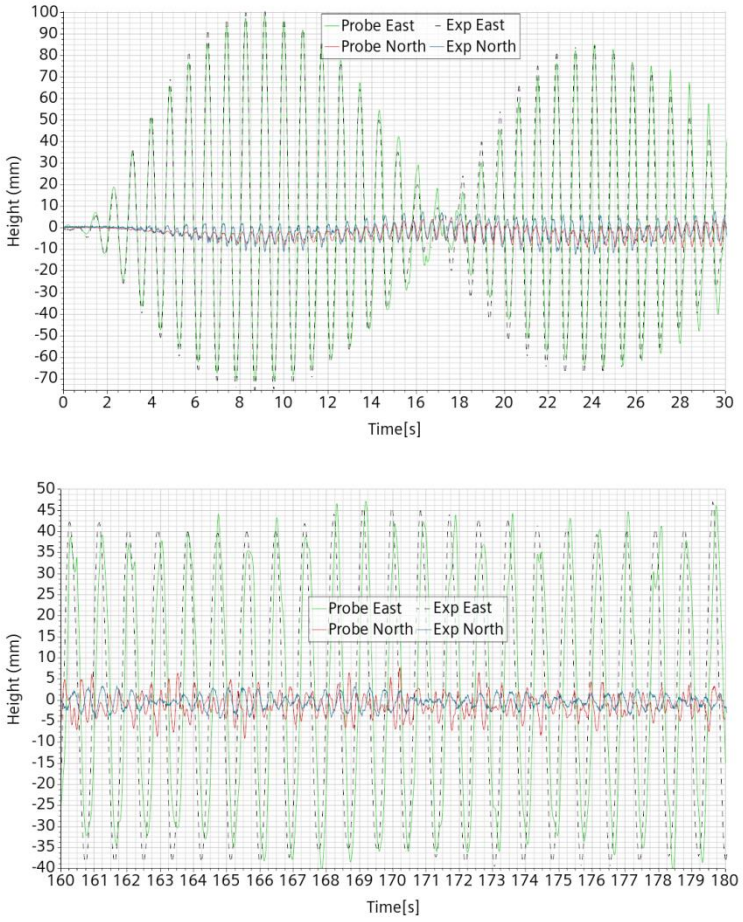


Figure 20. Reference case without adapted mesh and but with CFL control.

# 4.6 Physical setup dependency

## 4.6.1 Effect of increased viscosity

A comparison is performed with the exact same case apart from a viscosity raised to 3.E-3 Pa s. Some minor difference appears more clearly during the second modulation in which the augmented viscosity induces a slightly reduced maximum amplitude. This is illustrated in Figure 21.

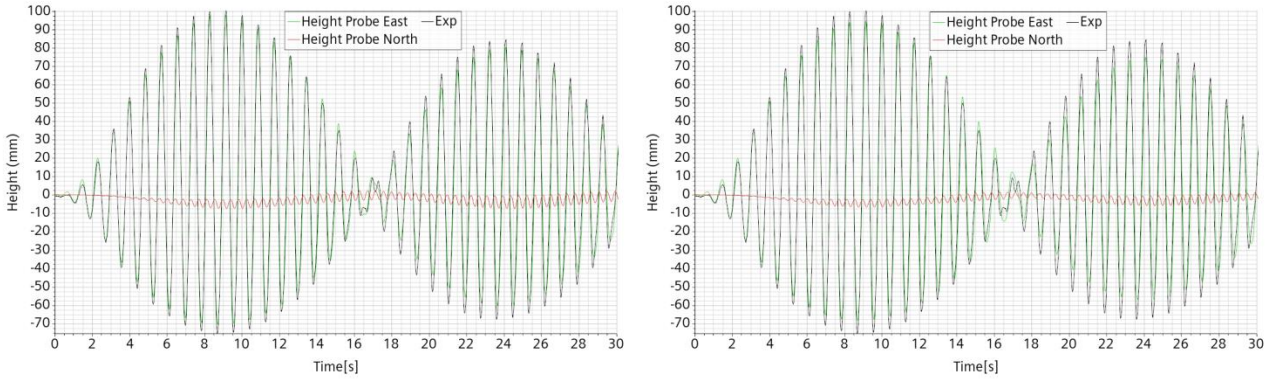


Figure 21. Reference case with two levels of adaptive refinement, left viscosity 1.E-3 Pa s, right viscosity 3.E-3 Pa s.

### 4.6.2 Effect of increased amplitude.

There is a discrepancy between the forcing amplitude imposed and the one measured, with this later being about 0.3 mm higher. However the measured amplitude is subject to some noise and so is its maximum. To estimate the possible error induced numerically, we redo the reference case with the amplitude raised from 3.98 to 4.20 mm.

The increase of forcing amplitude gives rise to an increase of the wave height and an increase of the modulation maximum. The first modulation node is also neatly delayed. This is a clear confirmation that the SHAKSPEARE input signal is to be trusted rather than the measured one.

The comparison is performed with the full refined numerical setup as indicated a little later: 2 levels of mesh adaption and time step controlled by CFL and free-surface displacement.

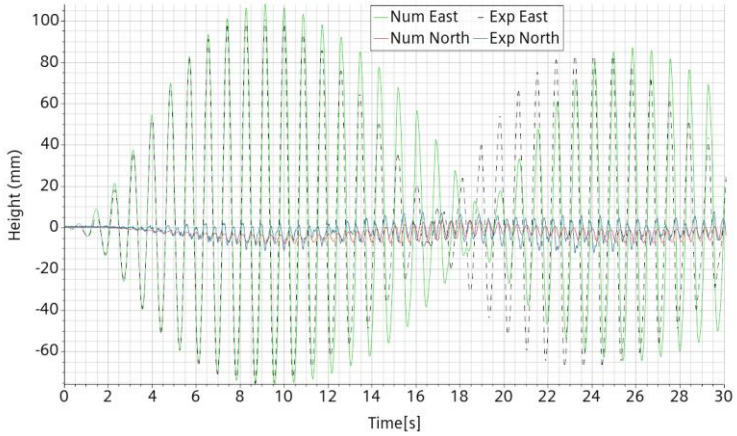


**Figure 22. Amplitude increased to 4.2 mm with two levels of adaptive refinement and viscosity 1.E-3 Pa s.**

## 4.7 Lower transition to chaos

Chaos arises numerically when the frequency is set to $0.925 f_0$, see Figure 23, slightly before the experiment in which is appears and only occasionally at $0.9255 f_0$. At $0.9275 f_0$, see Figure 24, the oscillation initially rises much higher numerically than experimentally, delaying somewhat the appearance of the perpendicular motion. However the global behavior is quite similar. We look here at what are the onset features of the transition by simulating also the frequencies $0.923 f_0$ and $0.924 f_0$, respectively Figure 25 and Figure 26.

To fix the ideas, a wave acceleration overcomes gravity when its maximum amplitude is about 190 mm.

It takes about 20 to 25 s for the $0.925 f_0$ simulation to clearly go critical, as shown on Figure 23 where the experimental probe height at $0.9255 f_0$ is also indicated for comparison.

In comparison with the reference case at $0.92 f_0$ the frequency increases to $0.923 f_0$ as the effect of increasing the maximum amplitude and to delay the first modulation node. This is practically identical to what happens when the forcing amplitude is slightly increased.

Increasing further the frequency to $0.924 f_0$, the maximum amplitude is further increased and the first node further delayed. This is perfectly consistent with the experiment showing the same

trend. We can thus conclude that the bifurcation is captured within 0.1% of the frequency. This is particularly impressive considering that around the bifurcation the experiment is not fully reproducible, probably due to long time surviving slow internal coherent recirculation flows.

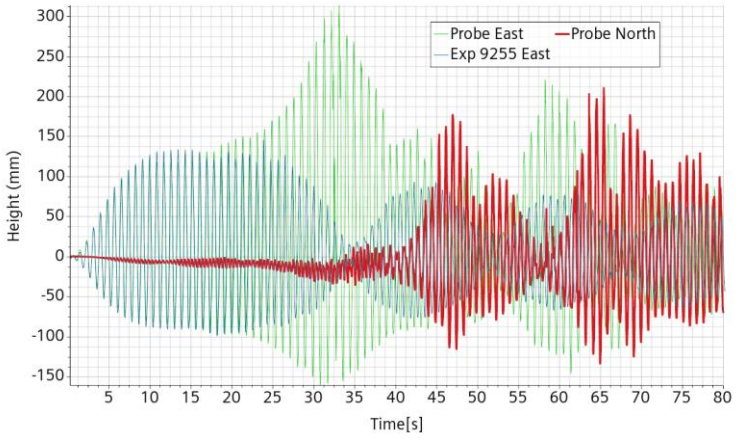


Figure 23. From reference case with two refinement levels and the frequency raised to 0.925$f_0$.

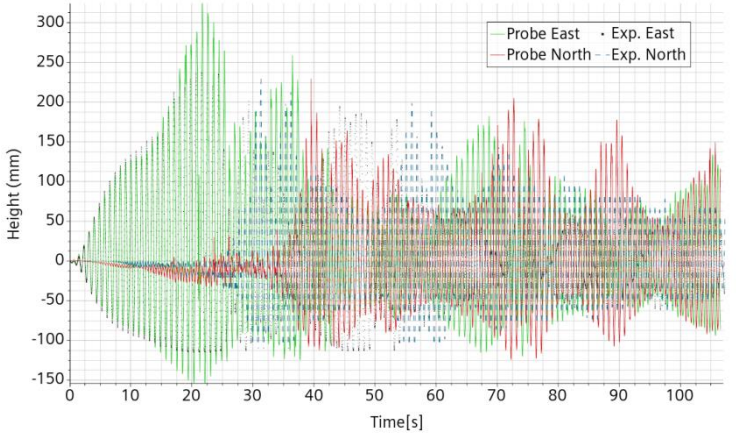


Figure 24. From reference case with two refinement levels and the frequency raised to 0.9275$f_0$

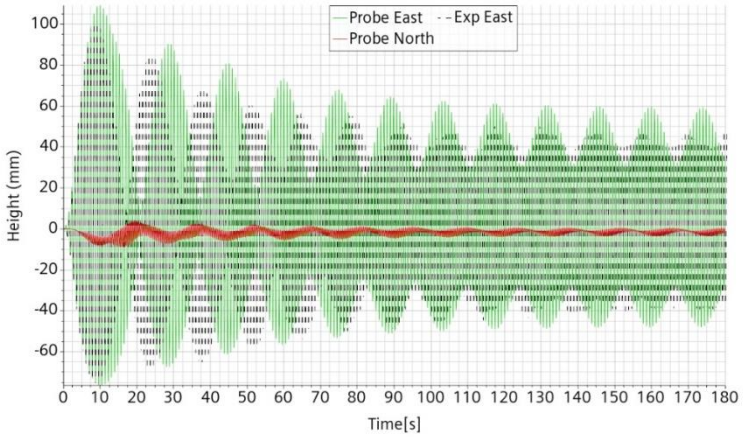


Figure 25. From reference case with two refinement levels and the frequency raised to 0.923 $f_0$.

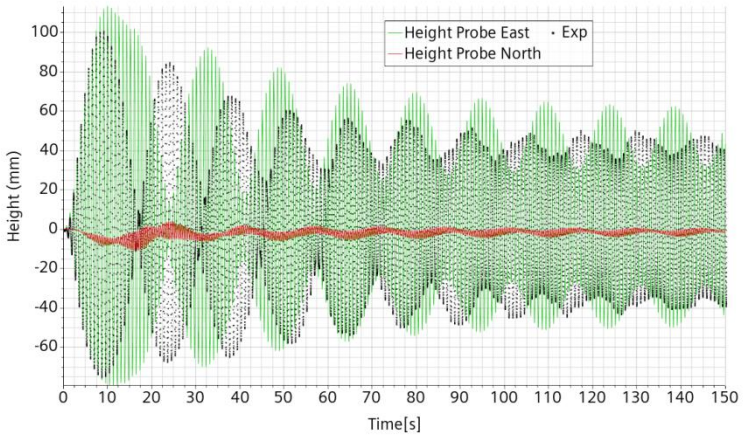


Figure 26. From reference case with two refinement levels and the frequency raised to 0.924 $f_0$.

# 5 The extrapolation issue

In the map shown in Figure 1 from [1], the bifurcation for the corresponding amplitude arises at about 94.5% of the first asymmetrical mode, while in our experimental setup it appears about 92.5%. This is further confirmed by the numerical simulation. This means that the map is much less universal than expected.

The main differences between the experiments is the radius of the water vessel. It is 7.8 cm in [1] and 29.8 cm, or about four times more in our case. As already noticed, the flow below the bifurcation is laminar. This means that it also critically depends on the viscous effects, or in adimensional form on the Reynolds number.

For the same fluid near resonance, the Reynolds number scales like the characteristic dimension $L$ of the vessel and the characteristic speed which scales like $L^{0.5}$ due to the combined effect of the larger height and the slightly lower frequency. That is, the Reynolds number for sloshing at a given percentage of the first asymmetrical mode scales like the power 1.5 of the radius. The SHAKESPEARE Reynolds number is about 7.5 times higher than the Hopfinger [1] one.

Anticipating the results of further simulations, we reproduce again Figure 1 with the addition of the results of our simulations giving the planar mode and the limit above which arises the chaotic mode, see Figure 27. No values are given in the swirling region because the simulations would require a much higher physical time to infer an asymptotic amplitude, if any would arise.

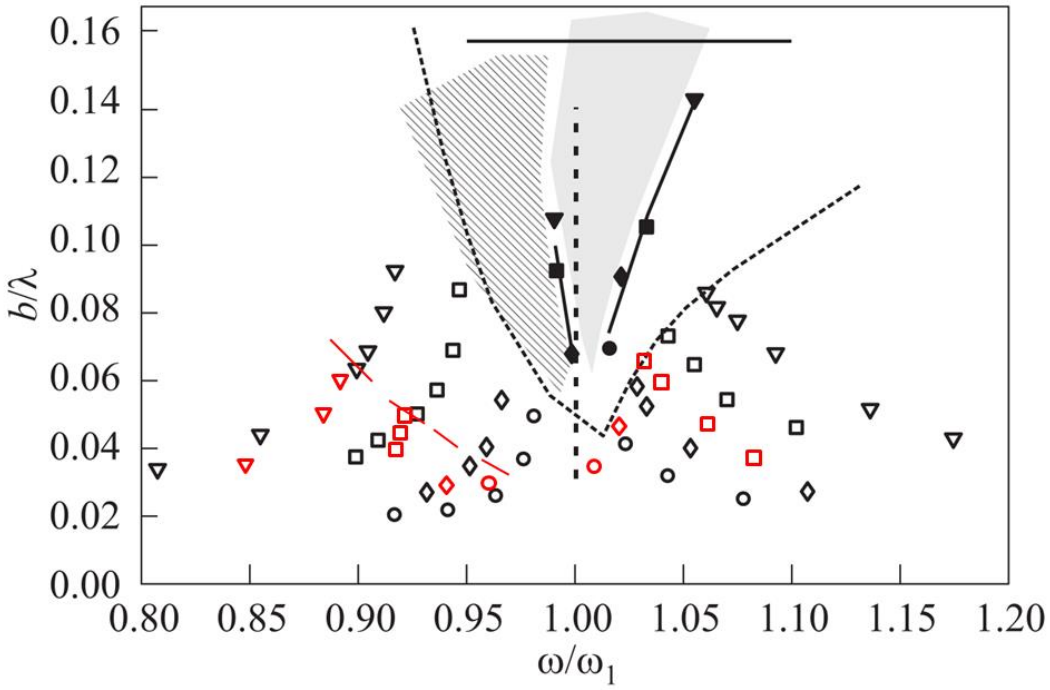


**Figure 27. Same as Figure 1, with the corresponding simulation values in red for the planar mode and vessel radius of ~30 cm. Above the dotted red line indicates where further simulations exhibit the chaotic mode.**

# 6 Additional boundary estimates

Now that the numerical setup is considered satisfying, we make some additional simulations to get a better idea of the envelop of the different sloshing modes. For frequencies below resonance, there is an abrupt transition from the planar more to the chaotic mode. Here, the chaotic mode is characterized by two different aspects: (i) breaking of the wave with formation of droplets and bubbles and (ii) alternate planar and swirling modes with the swirling modes also alternating sense of rotation.

For frequencies very slightly below and slightly above resonance, there is a swirling mode alternating with an almost planar mode but with swirling always in the same sense of rotation. The more we get close to the chaotic regime the more the almost planar mode develops.

For frequencies clearly above resonance, the planar more is found again. For frequencies slightly above resonance, the swirling mode may take quite a while to develop. But from literature, once developed, it is known to be very stable under frequency increase. This means also that the swirling mode depends on the initial conditions which cannot be totally controlled and on the path chosen for the forcing. For this reason, the establishment of very precise asymptotic mode boundaries in this frequency region is not really meaningful.

## 6.1 At resonance $f_0$

At resonance we choose to decrease progressively the forced displacement amplitude starting from 2 mm down to 1 mm. We can see that the flow always enters the swirling mode in the

forcing range [1-2] mm however the time to enter the swirling mode increase with the decrease of the forcing amplitude. This is illustrated in the following.

### 6.1.1 Displacement 2 mm.

First peak amplitude at 113 mm. No bifurcation before the second modulation minimum at about 50 s. Then bifurcation occurs. Run for 180 s. Large variations of both amplitudes but no change in the rotation direction. So the mode is rather swirling than chaotic.

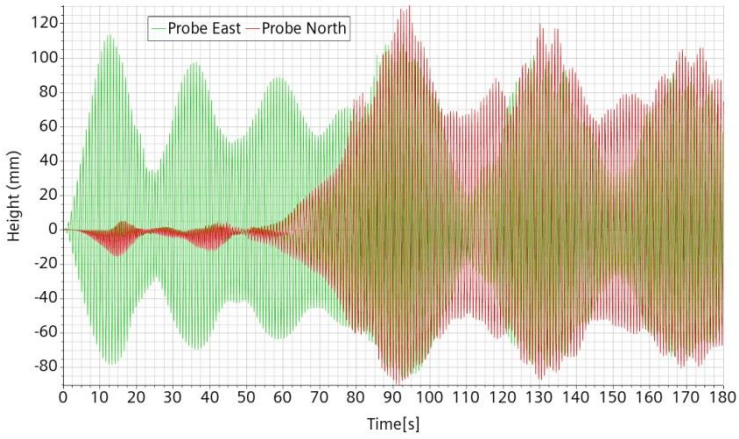


Figure 28. Reference mesh and setting, $f$ = 1.0 $f_0$, $A$ = 2.0 mm.

### 6.1.2 Displacement 1.8 mm

First peak amplitude at 107 mm. Minimum after the second peak at about 50 s. Then bifurcation. Run for 138 s.

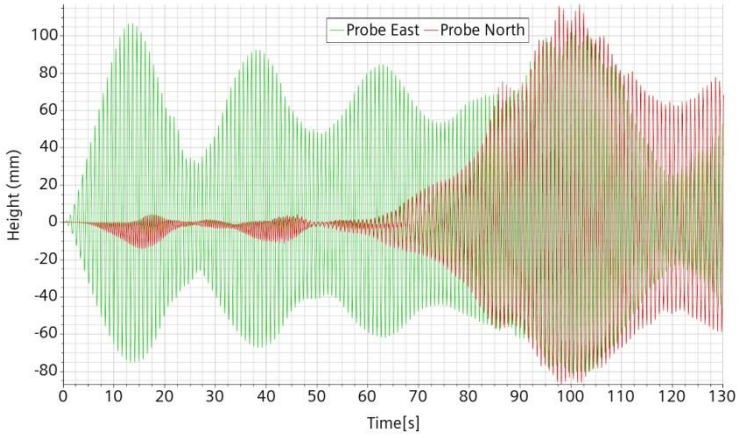


Figure 29. Reference mesh and setting, $f$ = 1.0 $f_0$, $A$ = 1.8 mm.

### 6.1.3 Displacement 1.5 mm.

First peak amplitude at 96 mm. The local minimum after the second maximum happens at about 60 s. Bifurcation occurs after about 70 s. Run for 110 s.

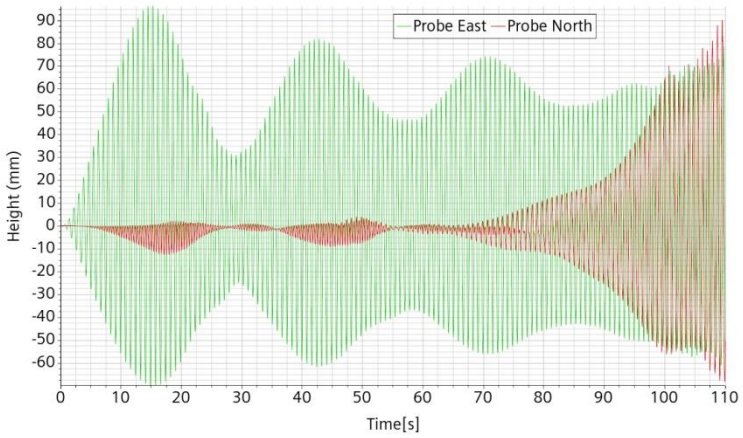


Figure 30. Reference mesh and setting. $f$ = 1.0 $f_0$, $A$ = 1.5 mm.

### 6.1.4 Displacement 1.0 mm

First peak amplitude at 74 mm after 56 s. Second local minimum after 78 s. Bifurcation starts after ~85 s. Run for 178 s. Apparent stable swirling mode. No test for even lower displacement because potential bifurcation, if ever, would be very long to appear.

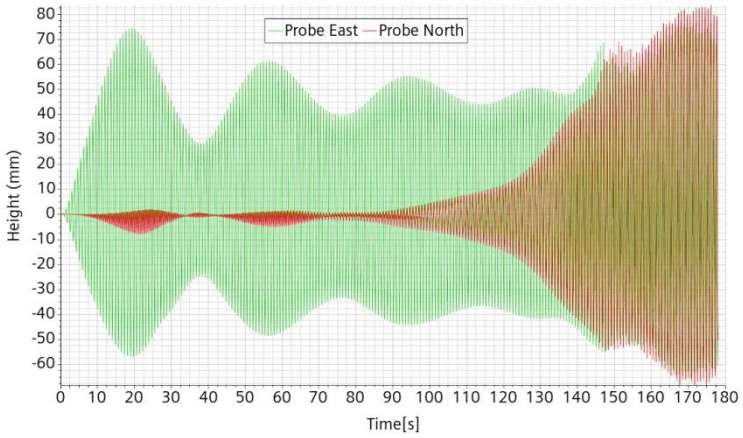


Figure 31. Reference mesh and setting. $f$ = 1.0 $f_0$, $A$ = 1.0 mm.

## 6.2 At 3.98 mm displacement for f > f₀

The objective is to capture the bifurcation from planar to circular mode, starting from an a priori high enough frequency and then running successive simulations with lower frequencies. We found the bifurcation very close to $1.025 f_0$ with an asymptotic amplitude near 75 mm. Experimentally, the bifurcation occurs "sooner" at about $1.035 f_0$. This may due to the combined effect of the stability of the swirling mode and the impossibility to start the experiment with a fluid sufficiently at rest.

### 6.2.1 f = 1.08 f₀

The first modulation peak is at about 68 mm far from the apparent critical value around 110 mm. Run for 68 s. Asymptotic amplitude estimated about 35 mm.

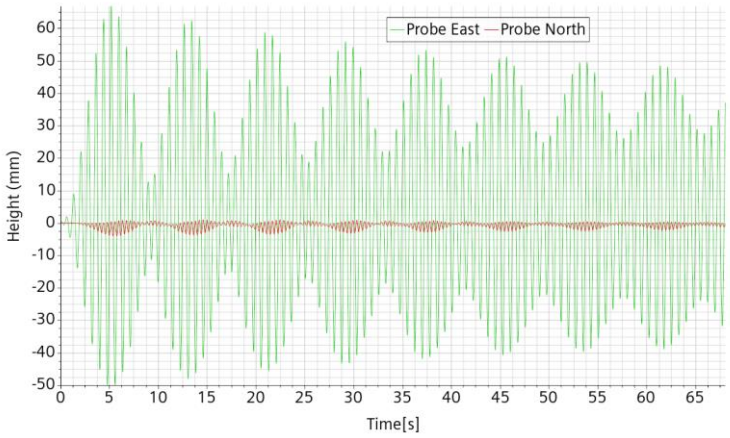


Figure 32. Reference mesh and setting. $f$ = 1.08 $f_0$, $A$ = 3.98 mm.

### 6.2.2 f = 1.06 f0

Run for 140 s without showing onset of bifurcation. Asymptotic amplitude about 46 mm.

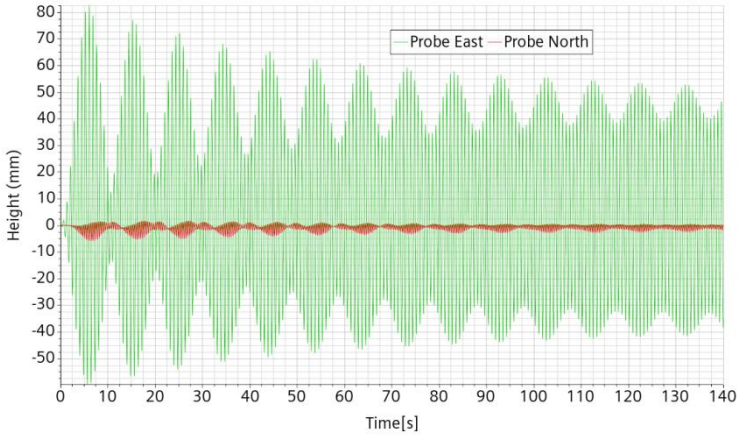


Figure 33. Reference mesh and setting. $f$ = 1.06 $f_0$, $A$ = 3.98 mm.

### 6.2.3 f = 1.04 f0

Run for 140 s without showing onset of bifurcation. Asymptotic amplitude about 60 mm.

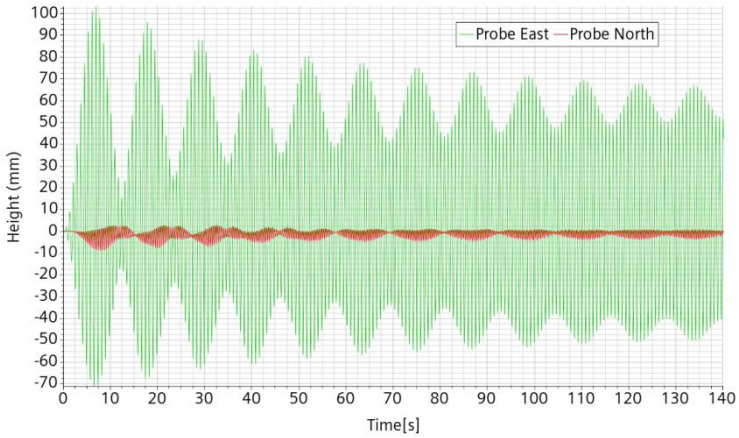


Figure 34. Reference mesh and setting. $f$ = 1.04 $f_0$, $A$ = 3.98 mm.

### 6.2.4 f = 1.03 f$_0$

First modulation at 112 mm. No bifurcation for the first 180 s. Some tiny orthogonal displacement between 75 s and 130 s, dying afterward. Seemingly asymptotic amplitude about 67 mm.

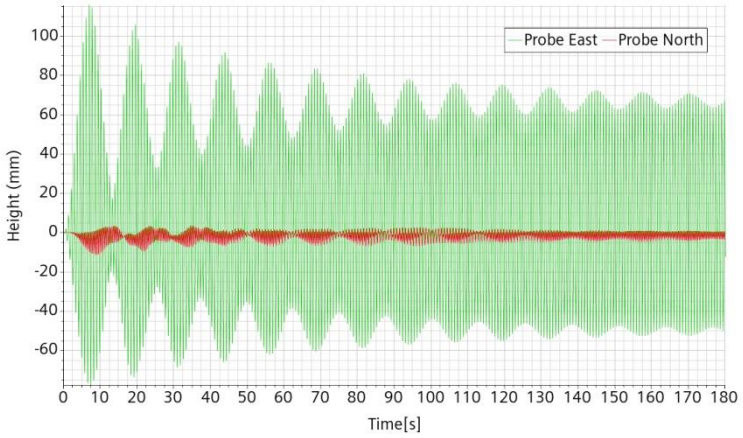


Figure 35. Reference mesh and setting. $f$ = 1.03 $f_0$, $A$ = 3.98 mm.

### 6.2.5 f = 1.02 f$_0$

First modulation peak at 130 mm then bifurcation after 70 s. Run for 162.7 s. Seems to converge towards a stable swirling motion, but still modulated.

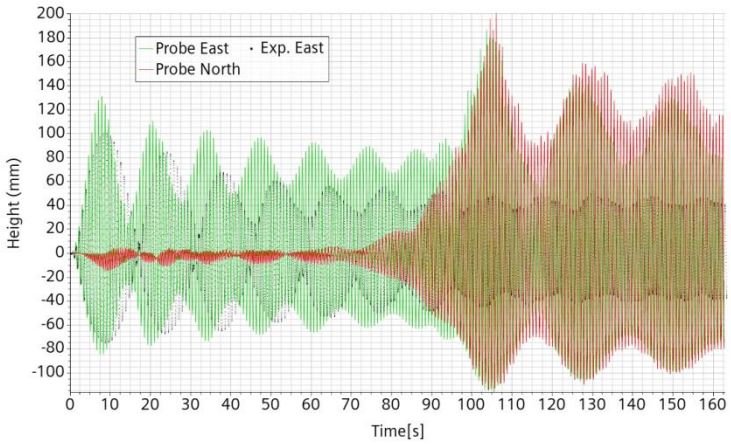


Figure 36. Reference mesh and setting. $f$ = 1.02 $f_0$, $A$ = 3.98 mm.

### 6.2.6 f = 1.025 f$_0$

First modulation maximum at 122 mm after 7.8 s. Top amplitude tends to stabilize at about 70 mm. After about 120 s a very slight change in the North-South small oscillation occurs. The oscillation then grows very slowly at first then more and more rapidly up to a maximum of 192 mm at 236 s. Run until 240 s. During the North-South increase, the East-West oscillation remains very stable at 75 mm up to 200 s then follow the same trend as the North-South one.

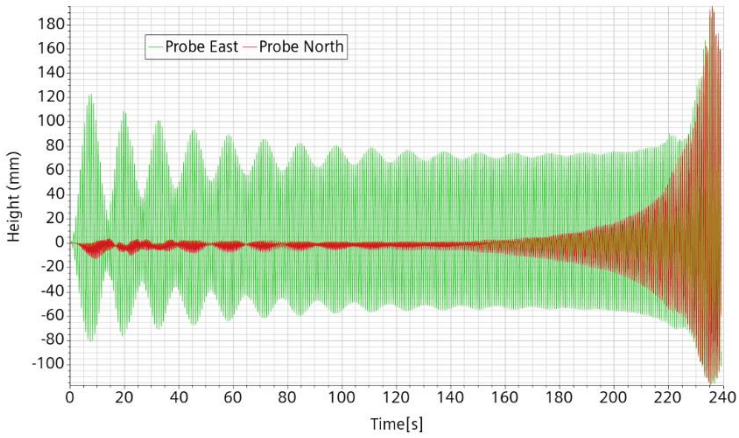


Figure 37. Reference mesh and setting. $f$ = 1.025 $f_0$, $A$ = 3.98 mm.

## 6.3 At f = 0.9275 $f_0$, 3.98 mm displacement

Experimentally, this case gives a very high amplitude from the beginning leading to splashing and further chaos behavior. Numerically, the behavior is quite similar. We must acknowledge that when the wave becomes high, its tip is no longer in the refined region and even if there still are two levels of adaptive refinement, the cell size remains much larger than below. This cuts the possibility to make accurate small droplets and creates de facto a more smeared interface. Moreover, with very large displacements, it is unlikely that the flow remains laminar so that when the wave becomes very high, the accuracy of the simulation becomes questionable. Run for 106.5 s.

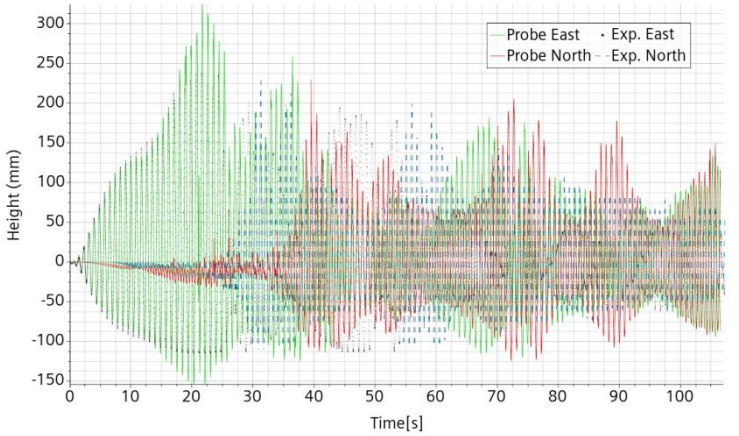


Figure 38. Reference mesh and setting. $f$ = 92.75 $f_0$, $A$ = 3.98 mm.

## 6.4 Displacement 2 mm.

Considering that bifurcation to chaos for 3.98 mm displacement appears quite before expected, we inquire whether this is also the case for a smaller amplitude. We thus run some simulations with imposed displacement amplitude of 2 mm.

### 6.4.1 f = 0.96 f₀

Runaway is clear from the beginning and a chaotic behavior seems to establish itself.

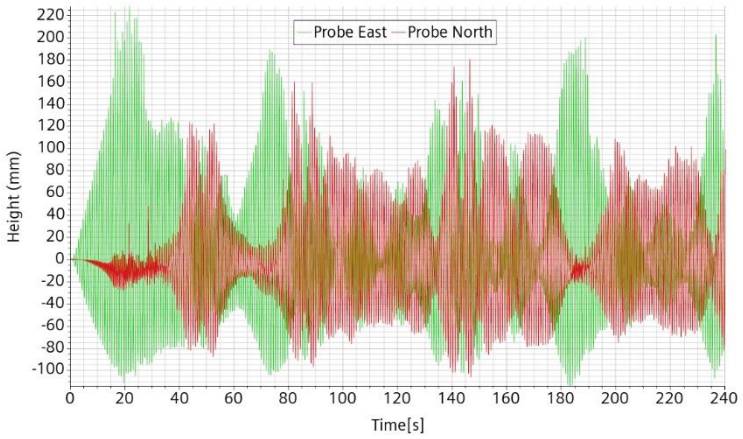


Figure 39. Reference mesh and setting, $f$ = 0.96 $f_0$, $A$ = 2 mm.

### 6.4.2 f = 0.95 f₀

It takes 20 s for the runaway configuration to take place. Orthogonal displacement develops after about 45 s. Then the chaotic mode develops.

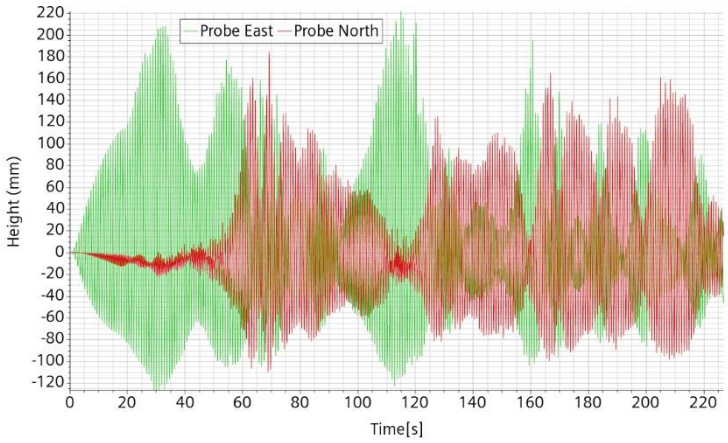


Figure 40. Reference mesh and setting, $f$ = 0.95 $f_0$, $A$ = 2 mm.

### 6.4.3 f = 0.94 f₀

The simulation is run for 220 s and the mode remains planar with asymptotic amplitude about 29 mm.

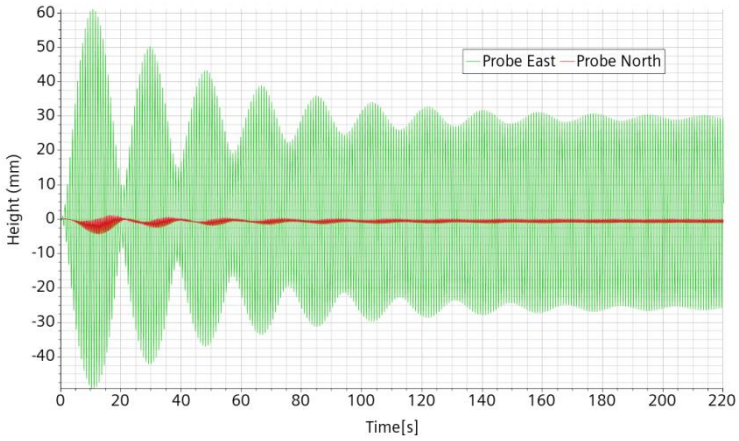


Figure 41. Reference mesh and setting, $f$ = 0.94 $f_0$, $A$ = 2 mm.

### 6.4.4 f = 1.04 f0

Simulation run for 140 s indicating planar mode and asymptotic amplitude about 58 mm.

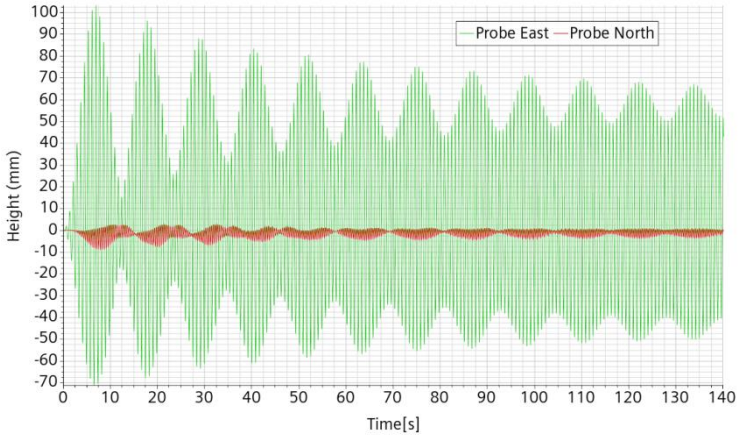


Figure 42. Reference mesh and setting, $f$ = 1.04 $f_0$, $A$ = 2 mm.

### 6.4.5 f = 1.02 f0

The simulation is run for 290 s as there was some tiny onset of asymmetrical orthogonal displacement, which however did not develop. It seems that we are close to a bifurcation. Asymptotic amplitude about 47 mm.

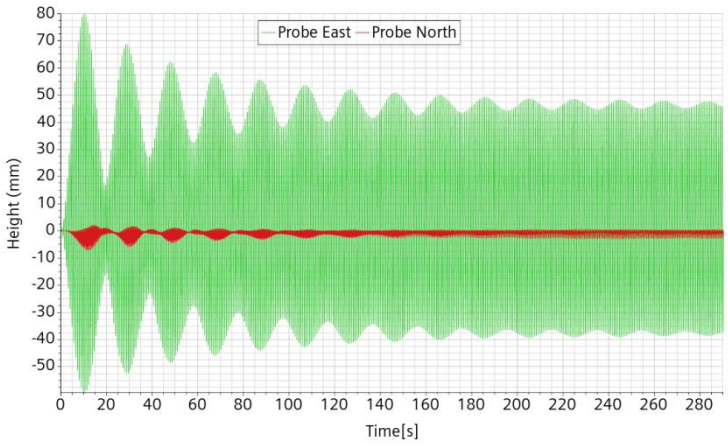


Figure 43. Reference mesh and setting, $f$ = 1.02 $f_0$, $A$ = 2 mm.

### 6.4.6 f = 1.01 f$_0$

It takes about 100 s before the flow slow bifurcation towards apparently swirling mode. The simulation is run for 180 s so the stability of the swirling mode or an asymptotic amplitude cannot be yet seen. The time to develop the bifurcation mode is interpreted as being very close to the stability boundary of the planar mode.

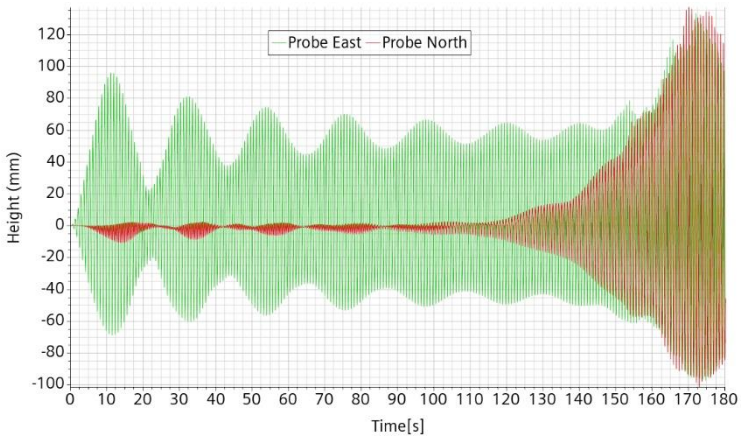


Figure 44. Reference mesh and setting, $f$ = 1.01 $f_0$, $A$ = 2 mm.

### 6.4.7 f = 0.99 f$_0$

It takes about 50 s to enter swirling mode alternating with slanted planar mode but initially not changing rotation direction. It changes direction after 140 s. This is interpreted as limit to the chaotic regime.

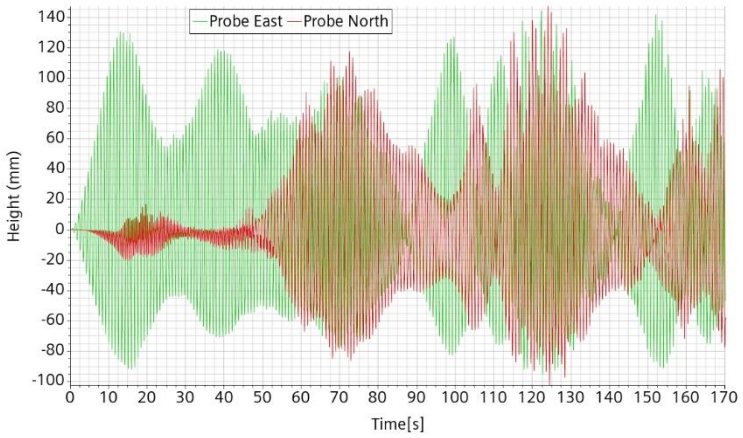


Figure 45. Reference mesh and setting, $f$ = 0.99 $f_0$, $A$ = 2 mm.

### 6.4.8 f = 0.98 f0

The first peak is above 180 mm after ~17 s, then the flow enters the chaotic mode after 40 s with alternate rotation directions and planar modes.

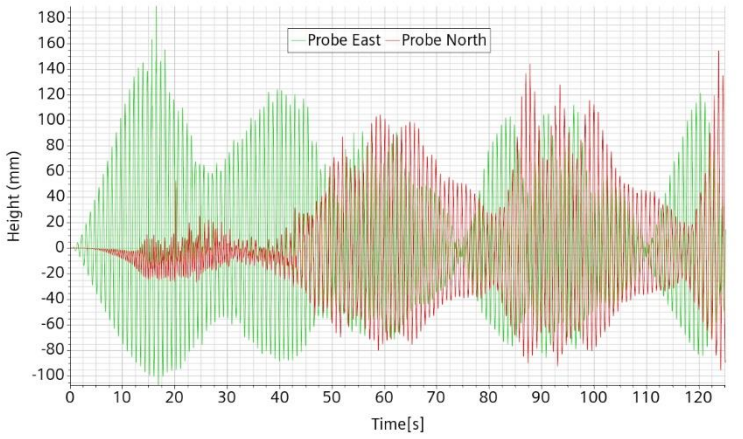


Figure 46. Reference mesh and setting, $f$ = 0.98 $f_0$, $A$ = 2 mm.

## 6.5 Displacement 1mm

To pursue the location of the bifurcation towards chaotic or swirling flow, we perform some simulations with the frequency very close to the resonance one and only 1 mm forcing amplitude.

### 6.5.1 f = 0.96 f0

The modulation decays quite rapidly and is negligible at the simulation end after 135 s. The mode is clearly planar.

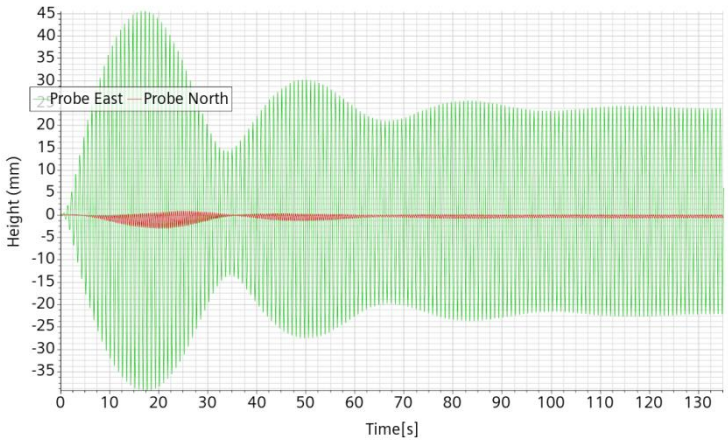


Figure 47. Reference mesh and setting, $f$ = 0.96 $f_0$, $A$ = 1 mm.

## 6.5.2 f = 0.97 f0

After about 50 s, it is clear that the flow will not pursue the planar wave mode. Then it enters a complex pattern typical of the chaotic flow. The simulation is run for 280 s.

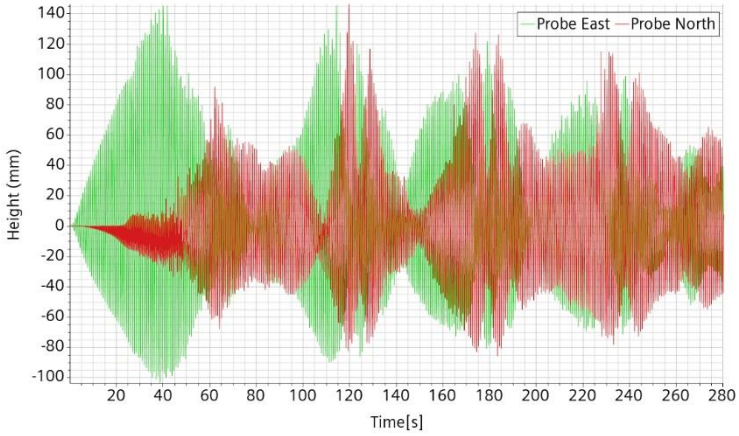


Figure 48. Reference mesh and setting, $f$ = 0.97 $f_0$, $A$ = 1 mm.

## 6.5.3 f = 0.98 f0

A clear bifurcation towards the chaotic mode appears after about 60 s. Then the flow enters a complex pattern typical of the chaotic flow. The simulation is run for 240 s.

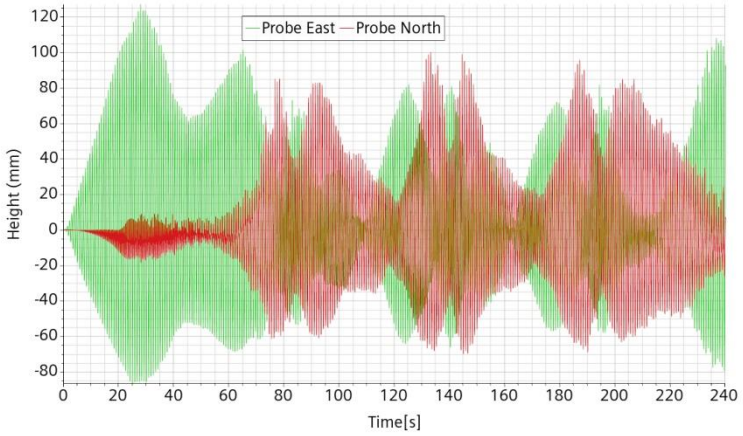


Figure 49. Reference mesh and setting, $f$ = 0.98 $f_0$, $A$ = 1 mm.

### 6.5.4 f = 0.99 f0

A clear bifurcation appears after about 60 s. It is not initially clear whether it is towards the swirling or the chaotic mode but at a later stage the probes register a behavior typical of the chaotic mode. The simulation is run for 240 s.

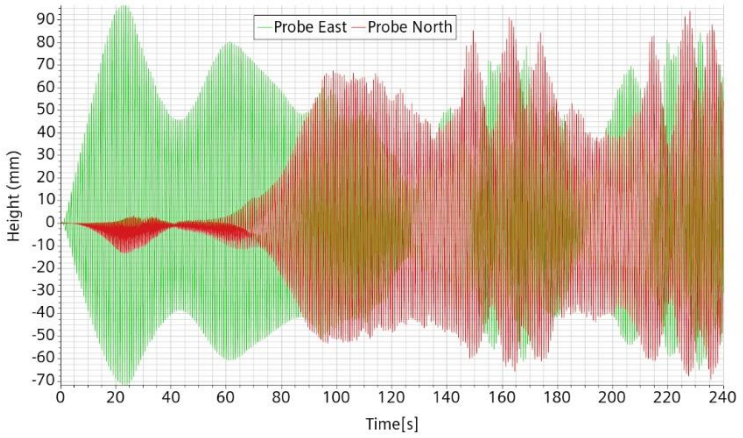


Figure 50. Reference mesh and setting, $f$ = 0.99 $f_0$, $A$ = 1 mm.

### 6.5.5 f = 1.01 f0

First peak at 56 mm after 15 s. Then for 150 s, the amplitude seems to slowly settle to 34 mm. From 105 s on, a tiny orthogonal signal slowly grows very slowly but eventually collapses after 220 s.

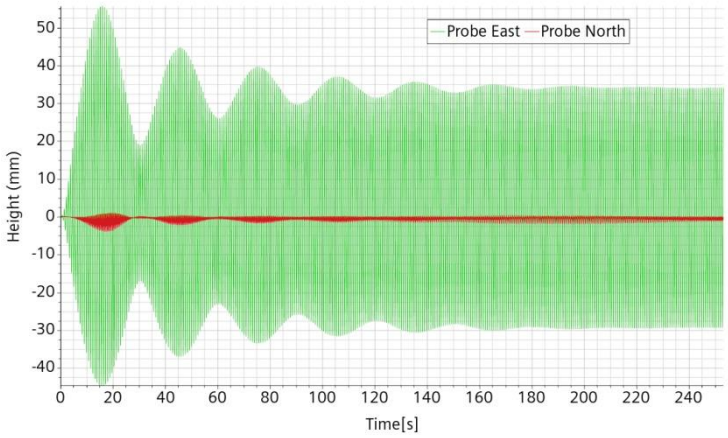


Figure 51. Reference mesh and setting, $f$ = 1.01 $f_0$, $A$ = 1 mm.

## 6.6 Displacement 8 mm.

A few additional simulations are performed with the maximum displacement ratio that can be compared with Figure 1. We want to determine the transition frequency from planar to chaotic mode and verify that the trend observed at lower forcing is confirmed.

### 6.6.1 f = 0.90 f□

The flow amplitude rises very fast up the lid with large wave breaking, bubbles formation and droplets ejection

### 6.6.2 f = 0.85 f□

The flow is clearly in planar mode with an asymptotic amplitude about 36 mm quite below the reference one at an equivalent about 45 mm. With the previous simulation, we get a preliminary envelop for the transition that we now try to refine.

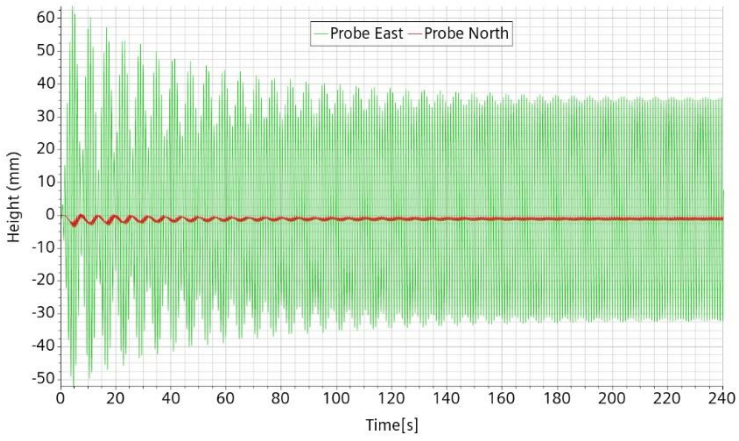


Figure 52. Reference mesh and setting, $f$ = 0.85 $f_0$, $A$ = 8 mm.

### 6.6.3 f = 0.88 f□

The flow remains in planar mode with a first peak at 106 mm after 6 s and an asymptotic amplitude about 50 mm.

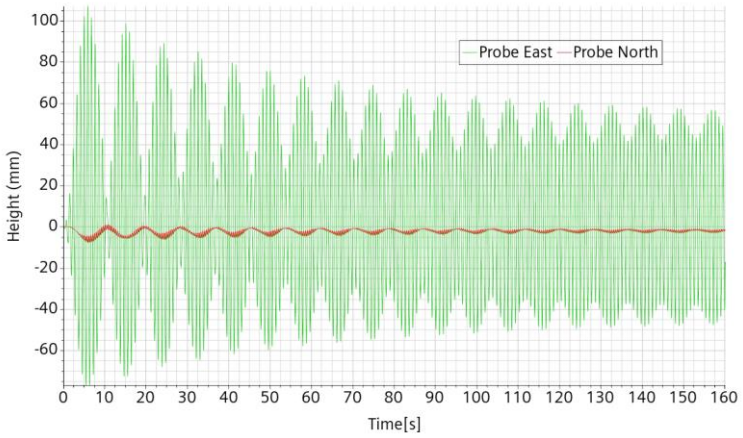


Figure 53. Reference mesh and setting, $f$ = 0.88 $f_0$, $A$ = 8 mm.

### 6.6.4 f = 0.89 $f_0$

The flow seems to remain in planar mode. First peak at 130 mm after 6.7 s. Asymptotic amplitude near 59 mm.

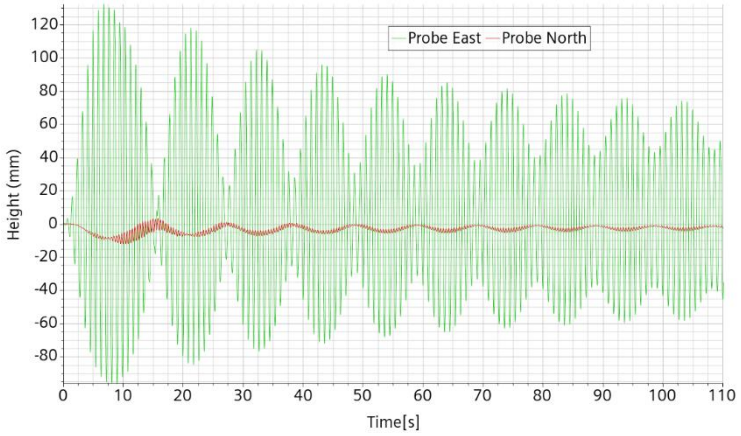


Figure 54. Reference mesh and setting, $f$ = 0.89 $f_0$, $A$ = 8 mm.

### 6.6.5 f = 0.895 $f_0$

The flow runs wild from the start reaching an amplitude of 300 mm in 15 s and subsequent wave breaking.

# 7 Conclusions

We have checked that CFD was qualified to simulate the sloshing phenomena. For this, it was decided to set an experimental campaign consisting in a water cylinder of 60 cm diameter with flat bottom filled up to 45 cm, solicited by a sinusoidal horizontal linear forcing with frequencies spanning around the first asymmetrical natural mode $f_0$ = 1.236 Hz and with 4 mm amplitude. From the experimental test at 0.92 $f_0$, it was found out that

- turbulence setup is excessively dissipating and must be discarded;
- the laminar setup can be accurate;
- the flow is very sensitive to the forcing characteristics;
- the free-surface must be accurately discretized for acceptable numerical matching.

Under these conditions, a very good reproduction of the experimental flow could be obtained.

There is a precise transition frequency across which the planar flow becomes chaotic with a fast and large initial amplitude growth up to wave breaking. The experimental bifurcation value is 0.9255 $f_0$. Numerically the value is found somewhere inside the interval [0.924, 0.925] $f_0$, that is within 0.1% of the experimental value. This result is a clear validation of the CFD modelling.

The transition frequency is quite far away from the one expected from literature, above 94%, found with a much smaller tank of 7.8 cm radius. This means that the transition frequency changes with the tank radius in such a way that the chaotic region in the phase parameter map grows with the radius. The 60 cm water tank diameter was chosen as the largest one easy to handle by SHAKESPEARE, so that surface tension effect on the natural frequency is totally negligible, and the results could be safely extrapolated to much larger dimensions representative of ALFRED or MYRRHA. It turns out that we now know that it is not the case.

Probably related to the transition frequency change, larger vessel radii lead to larger Reynolds numbers and more likelihood to have a turbulent flow for which the current CFD modelling is not suited.

The CFD modelling has been calibrated on the 0.92 $f_0$ / 4 mm experiment. We need to know if the modelling remains valid in other configurations and has predictive capabilities. For this reason, several simulations have been performed to characterize the flow and in particular, to give estimates of the bifurcation value at different forcing amplitudes. At the moment of writing the conclusions (May 2023), the corresponding experiments have not been performed. They have some likelihood to be performed during summer and could validate further or invalidate the current CFD modelling.

# References

[1] E. J. Hopfinger and V. Baumbach, “Liquid Sloshing in cylindrical fuel tanks” Progress in Propulsion Physics 1 (2009) 279-292 DOI: 10.1051/eucass/200901279.

[2] Aude Royon-Lebeaud. Ballottement des liquides dans les réservoirs cylindriques soumis à une oscillation harmonique: régimes d’onde non-linéaire et brisure. Mécanique [physics.med-ph]. Université Joseph-Fourier - Grenoble I, 2005. Français.

# Appendix A: Smooth connecting functions

The objective of this part is to help deriving a sound reference test case for sloshing using the SHAKESPEAR seismic table at VKI and its numerical counterpart.

Taking input from the literature, we can choose a sinusoidal 1D excitation near the first asymmetric resonance mode. It is known than at sufficient amplitude, the asymmetric oscillation can transforms after a (short) while of a few seconds in a modulated rotatory motion. However, at lower forcing amplitudes, the secondary modes are not activated.

With this approach, we can be faced with an initial value problem. In absolute and in exact math, starting from flow at rest, and with 1D oscillation, the asymmetric mode is activated but transfer to the rotational mode cannot appear. In practice, the rotational mode is indeed activated because the liquid can never be completely and absolutely initially at rest and because absolute axial-symmetry and verticality of the setup is obtained only within a certain tolerance. The number of periods necessary to have a relevant transfer to the rotational mode depends however on this unknown residual component, or shape/positional defect. Numerically, it depends on the quality of the initial condition and maybe also of the non-perfectly cylindrical geometrical discretization. It is thus impossible to have a good experimental-numerical matching during all the initial transition phase.

In order to remedy, we need to gain a better control on the initial condition and bring the system in a controlled way in a configuration in which the asymmetric mode is already measurably activated, that is giving for a short time some displacement in the orthogonal direction. This is not necessary if no bifurcation behavior is expected.

A better control is obtained with smooth displacements which are also more easily reproduced numerically. Smooth displacements are expected not to excite strongly high resonance modes difficult to capture numerically.

The SHAKESPEARE table is activated through excel files indicating displacement at 100 Hz.

Our current objective is to exhibit a set of functions allowing to smoothly connect the initial condition at rest to a periodic 1D horizontal oscillation centered on the initial position. The connection is due to happen after exactly a small integer multiple of one period. During this time, displacement in the orthogonal planar direction must go back to the initial position for a 1D periodic movement.

We need the time displacement functions $\big(X(t), Y(t)\big)$, and check that the corresponding velocities $\big(V_x(t), V_y(t)\big)$ and accelerations $\big(A_x(t), A_y(t)\big)$ all match the periodic motion after a small number $N$ of period $T$.

Notation: time $t$, period $T$, frequency $f$ and angular frequency $\omega$. The triplet $(T, f, \omega)$ is connected by the relation $\omega = 2\pi/T = 2\pi f$.

For commodity, we consider a unit displacement amplitude. After $N$ periods, we are supposed to have:

$$\big(X(t), Y(t)\big) = (\sin(\omega t), 0)$$

Continuity and smoothness at the initial displacement time implies:

$$X(0) = Y(0) = V_x(0) = V_y(0) = A_x(0) = A_y(0)$$

At time $t = NT$:

$$\big(X(NT), Y(NT)\big) = (0,0)$$

$$\big(V_x(NT), V_y(NT)\big) = (\omega, 0)$$

$$\big(A_x(NT), A_y(NT)\big) = (0,0)$$

That is the position on the X-axis must turn back to zero but with speed $\omega$ and no acceleration.

The functions $X$ and $Y$ have each 6 constraints to fulfill. In principle, this can be done with a 5$^{th}$ order polynomial. This would be however of relatively difficult interpretation. Instead, through trial and errors, we have arrived to more easily interpretable simple trigonometric functions.

The function $X(t)$ defined by:

$$X(t) = A(t)\sin(\omega t)$$

with

$$A(t) = A_0 \sin^2(\omega t/4N)$$

$t$ in $[0, NT]$.

Giving in turn

$$V_x(t) = A_0\omega\left[\sin^2(\omega t/4N)\cos(\omega t) + \frac{1}{2N}\sin(\omega t/4N)\cos(\omega t/4N)\sin(\omega t)\right]$$

$$V_x(t) = A_0\omega\left[\sin^2(\omega t/4N)\cos(\omega t) + \frac{1}{4N}\sin(\omega t/4N)\sin(\omega t)\right]$$

where $N$ is the number of cycles in which we want to reach the asymptotic amplitude.

$X(t)$ satisfies all 6 constraints (3 at time $t$ = 0 and 3 at time $t = NT$).

The $Y$ function must connect both sides of the interval of application with the null function.

Moreover the transversal kick (the $Y(t)$ function) can be delayed until the transitory $X(t)$ is finished. It can be done just on one side or involve both sides. Several choices are possible, such as:

$$Y(t) = \sin^3(\omega t/2N)$$

or

$$Y(t) = \sin^3(\omega t/2N)\sin^3(\omega t)$$

Conversely, for damping after $n$ periods $T$, we can take

$$A(t) = A_0 \cos^2(\omega(t - nT)/4N)$$

which will bring back smoothly the displacement do zero in $N$ periods.

In practice, in the VKI implementation, the square in the $A(t)$ definition has been omitted, leading to small discontinuities (of $A_0\omega^2/2N$) of the acceleration but also to a simpler formula for the velocity: if

$$A(t) = A_0 \sin(\omega t/4N)$$

$t$ in $[0, NT]$, then

$$V_x(t) = A_0\omega \left[\sin(\omega t/4N)\cos(\omega t) + \frac{1}{4N}\cos(\omega t/4N)\sin(\omega t)\right]$$

$t$ in $[0, NT]$.

Numerically, it is possible to implement the table oscillation either as a displacement or as a velocity.